RADIATIVE TRANSFER CHARACTERIZATION OF INHOMOGENEOUS

BOUNDARY LAYERS AT GALE CRATER, MARS

A Thesis

by

DOMINIC MICHAEL CARTINA

Submitted to the Office of Graduate and Professional Studies of
Texas A&M University
in partial fulfillment of the requirements for the degree of

MASTER OF SCIENCE

Chair of Committee,	Mark Lemmon
Committee Members,	Anita Rapp
	Casey Papovich
Head of Department,	Ping Yang

May 2017

Major Subject: Atmospheric Sciences

ABSTRACT

Dust aerosols in the Martian atmosphere play a fundamental role in determining the behavior of atmospheric circulations at all spatial scales and are well-known as a tracer of boundary layer dynamics. Vertical variations in atmospheric dust mixing ratios have recently been detected at Gale Crater, Mars, by the Mars Science Laboratory (MSL) rover, Curiosity, and have been interpreted in terms of the height of the planetary boundary layer (PBL) and local to mesoscale mixing processes. These variations have been observed though the use of a simplified radiative transfer analysis that utilizes Navigation Camera (Navcam) images of distant features to discern the near-surface dust mixing ratio along a defined line-of-sight. However, the simplified methods of radiative transfer established possess substantial weakness within the principal assumptions.

In order to assure that landed spacecraft for both present and future operations possess the robust capability of determining line-of-sight atmospheric optical depth, a three-dimensional radiative transfer model was developed to produce simulated atmospheric data that enabled the simplified methodology for measuring dust content to be evaluated and validated while limiting the number of required free parameters. In this model, the radiative transfer equation (RTE) was integrated over a line-of-sight in an arbitrary atmosphere that is a set of spherical shells and is horizontally homogeneous except for the existence of an idealized crater with allowed in-crater versus out-of-crater differences. The first-order scattering contribution to the RTE was calculated analytically. However, the multiple-scattering contribution was more complex and utilized numerous runs of the Discrete-Ordinate-Method Radiative Transfer (DISORT) numerical algorithm which characterized the diffuse radiation field as a function along the arbitrary Navcam line-of-sight. This work tests the simplified method under a variety of geometries and over the range of

relevant wavelengths in order to identify the existence of specified limitations that could alter and/or further develop the previously established observations within Gale Crater.

DEDICATION

This thesis is dedicated to my father, mother, brother, and girlfriend, as well as all of my friends and family, who have continuously supported me and encouraged me to achieve every goal that I possess.

ACKNOWLEDGMENTS

First and foremost, I would like to thank my advisor Dr. Mark Lemmon, for his constant help, guidance, and patience throughout the course of my graduate school career. I would also like to thank the members of my committee, Dr. Anita Rapp and Dr. Casey Papovich, for their much appreciated support.

I would like to thank my parents, George and Joyce, my brother Dustin, my girlfriend Lauren, and all of my close friends and family for the constant support throughout the years that has driven me to become the person I am today.

Finally, I would like to thank Texas A&M University, the Department of Atmospheric Sciences, and all of my friends that I have made throughout my time in Aggieland that have helped me along the way.

CONTRIBUTORS AND FUNDING SOURCES

Contributors

This work was supported by a thesis committee consisting of Professors Mark Lemmon and Anita Rapp of the Department of Atmospheric Sciences and Professor Casey Papovich of the Department of Physics and Astronomy.

Funding Sources

NOMENCLATURE

AERONET	Aerosol Robotic Network
CCD	Charged Coupled Device
DDSM	Dust Devil Search Movie
DISORT	Discrete-Ordinate-Method Radiative Transfer
DN	Data Number
EDL	Entry, Descent, and Landing
EECams	Enhanced Engineering Cameras
η	Airmass
EV	Entry Vehicle
F^{+}	Diffuse upward-flux
F^{-}	Diffuse downward flux
FOV	Field of View
H	Scale Height of the Martian Atmosphere
I_{crt}	Intensity coming off of the distant crater
$I_{diff,\lambda}$	Diffuse spectral radiance
I_{G}	Average spectral radiance of the ground
I_{M}	Average spectral radiance of the mountains
I_{S}	Average spectral radiance of the sky
$I_{Top\ Crater}$	Intensity observed at the top of the crater rim
IDC	Instrument Deployment Camera
IDL	Interactive Data Language
IMU	Inertial Measurement Unit
J_{D}	Source function of scattered atmospheric dust

$J_{diff,\lambda}$	Source function of diffuse radiance
$J_{dir,\lambda}$	Source function of direct radiance
J_{total}	Total source function
JPL	Jet Propulsion Laboratory
L_s	Solar longitude
LTST	Local True Solar Time
MER	Mars Exploration Rovers
MSL	Mars Science Laboratory
μ	Cosine of the polar angle
NASA	National Aeronautics and Space Administration
Navcam	Navigation Camera
$\tilde{\omega}$	Single scattering albedo (SSA)
ω_{sfc}	Albedo of the Martian surface
P	Phase function
PBL	Planetary Boundary Layer
φ	Azimuth angle
PHOTONS	PHysics Optoelectronics and Technology of Novel Micro-resonator Structures
RGB	Red/Green/Blue
RMSE	Root-Mean-Square Error
RSM	Remote Sensing Mast
RTE	Radiative Transfer Equation
$S_{dir,\lambda}$	Direct Solar Radiation
Sol	A Martian solar day (24 hours, 39 minutes, 35.244 seconds)
τ	Atmospheric optical thickness

τ_{crater}	Optical thickness above the crater elevation
τ_{MSL}	Total optical thickness above the Curiosity rover
τ_{out}	Optical thickness outside of the crater
TOA	Top of Atmosphere

TABLE OF CONTENTS

1. INTRODUCTION

1.1 Overview

Mars has been a subject of investigation for over half a century. Since the early 1960's, numerous missions have been conducted sending various robotic spacecraft to flyby, orbit, land, and rove the surface in order to obtain perspectives of another planet that have yet to be seen. Throughout years of research, a vast amount of information has been collected in the form of images and sensor measurements to further develop an understanding of the chemical and physical atmospheric processes that are comparable to patterns witnessed on Earth.

Radiative properties and the concentrations of atmospheric constituents play a significant role in determining the general behavior of the atmosphere; therefore, being able to model and study radiative transfer and energy transport of the Martian atmosphere possesses great importance for numerous applications (*Sportisse*, 2010). Specific radiative properties of atmospheric aerosols including particle mean size, phase function, single-scattering albedo, optical depth, and source function amongst many others that are necessary for atmospheric modeling, have been able to be measured with much higher precision with the advent of in situ spacecraft observations. The retrieval of these parameters through the use of a diverse collection of cameras has lead to significant improvements in atmospheric modeling as well as the overall understanding of Martian dust interactions. With the constant influx of measurements and discoveries provided from various robotic spacecraft, the current understanding of both past and present atmospheric processes on Mars continues to grow and will do so for the foreseeable future.

1.2 The Martian Atmosphere

The current gaseous atmosphere of Mars is primarily composed of carbon dioxide (approximately 96% by volume), with smaller quantities of argon (1.93%), nitrogen (1.89%), and trace amounts of other constituents such as water vapor, oxygen, and ozone (*Mahaffy et al.*, 2013; *Read et al.*, 2015). The Martian atmosphere is very thin and tenuous such that the average atmospheric pressure measures roughly 600 Pascals at the surface. Although the atmosphere possesses a pressure less than 1% of Earth's, it is still substantial enough to host a variety of reoccurring weather phenomena analogous to terrestrial observations. Clouds, fog, dust devils, as well as dust storms, have all been observed from both orbiting and ground-based spacecraft. Another meteorological phenomenon that occurs seasonally in the Martian atmosphere is snow, which has been observed in both water-ice and carbon dioxide forms near the northern and southern polar ice caps, respectively. The alternation between the winter deposition and the consequent sublimation at the poles significantly influences global circulation patterns and the transport of water vapor and dust.

1.3 Dust on Mars

Airborne dust on Mars is ubiquitous as there is a consistent presence of suspended particles of iron oxide and other minerals in the atmosphere. The optical properties of the dust are predominantly influenced by the high concentration of poorly crystalline or nanophase ferric oxides which are analogous to terrestrial palagonites or the mafic weathering products of basaltic glass (*Baird et al.*, 1976; *Allen et al.*, 1981; *Morris et al.*, 1993; *Bell et al.*, 2000; *Johnson et al.*, 2003). These ferric oxides dominate the spectral properties in the near-UV and visible wavelengths, giving Mars its distinctive reddish hue; however, their primary physical effect is their influence on the thermal structure of the atmosphere. Martian dust provides localized heating to the atmosphere through absorption of solar radiation, especially at 400 to 600 nm, as well as thermal radiation, especially near 9μm

(*Lemmon et al.*, 2004; *Fenton et al.*, 2016). Due to this influence on the radiative balance, the dust particles, in turn, strongly influence atmospheric circulations at all spatial scales.

Martian atmospheric circulations at the microscale are highly energetic, owing to high thermal contrasts, short radiative time scales, low atmospheric density, and steep topographical gradients (*Spiga and Forget*, 2009). Furthermore, at the microscale, daytime convective turbulence plays a significant role in atmospheric dynamics and is responsible for mobilizing, lifting, and maintaining the quantity of dust found in the Martian atmosphere. Loose surface sediment can also be lifted into the atmosphere through local mechanisms such as 'dust devils'. These transient convective vortices are thermally driven, forming through the process of differential surface heating and further contributing to the background atmospheric opacity (*Cantor et al.*, 2006; *Greeley et al.*, 2006; *Kahre et al.*, 2006; *Moores et al.*, 2015). Dust devils have been observed to occur somewhere on the Martian surface throughout every season; however, the majority of dust devil activity has been found to occur during the spring and summer seasons in the southern hemisphere (*Forget et al.*, 1999; *Cantor et al.*, 2006).

Coinciding with the increase of dust devil activity is the onset of the "dust storm season" which is observed when Mars is near perihelion or the time in which the planet's orbit is passing closest to the Sun. This close approach in Mars' eccentric orbit successively allows for surface temperatures to attain their peak values (*Martin and Zurek*, 1993). Furthermore, it is theorized that a positive feedback loop is established at this time through the absorption of incoming solar radiation by the airborne dust particles (*Haberle et al.*, 1993). As the dust particles absorb sunlight, they proceed to warm the surrounding air. The temperature of the air in the immediate vicinity of the dust increases; thus, the air becomes much warmer than the neighboring air. The increase in the local temperature gradient strengthens the pressure gradient force, which in turn generates or increases the wind velocity. The intensification of localized winds consequently lifts more dust from the
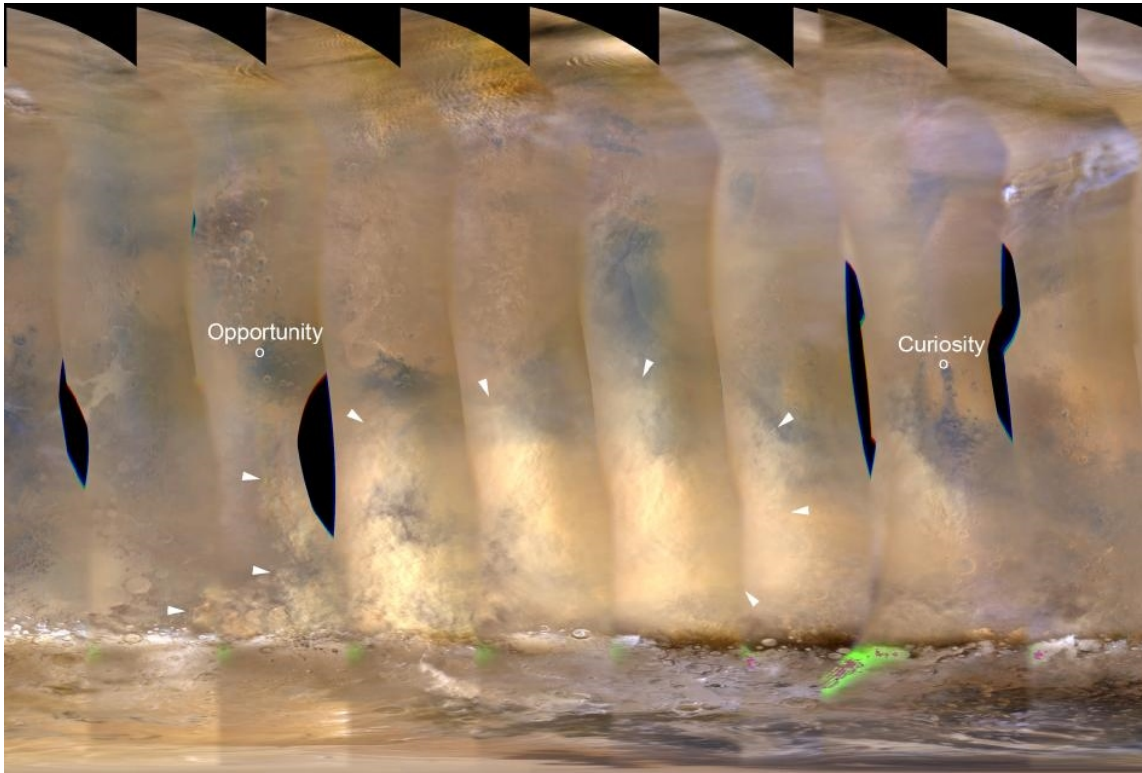
Figure 1.1: Nearly-global mosaic of observations of a regional-scale dust storm in the Martian southern hemisphere made by the Mars Color Imager aboard NASA's Mars Reconnaissance Orbiter on 18 November 2012. Image Credit: NASA/JPL-Caltech/MSSS

surface which further heats the atmosphere and continues to strengthen the winds (*Cantor et al.*, 2001).

The majority of Martian dust storms are local, being smaller than approximately 2,000 km across. They are commonly the result of enhanced local winds due to local topographical slopes, baroclinic waves, polar cap sublimation, and/or regional variations in thermal inertia (*Cantor et al.*, 2001). The typical lifespan of a local dust storm lasts about a few days as the intensification process is short-lived. However, it is possible for a collection of smaller, local scale storms to merge; therefore, expanding their coverage to a regional scale as seen in Figure 1.1. These storms have been defined as encompassing an area greater than 2,000 km while simultaneously lasting beyond a few days to upwards of three weeks.

Dust storms have also been known to encircle the planet; however, this occurs episodically and seems to have a one in three chance of occurring throughout any given Martian year (*Zurek and Martin*, 1993).

Martian atmospheric dust not only possesses a significant influence on energy transport and dynamics, but also poses a hazard for current and future robotic exploration vehicles. Previous studies have indicated that suspended dust particles in the Martian atmosphere have a mean radius of roughly 1.5μm (*Pollack et al.*, 1995; *Markiewicz et al.*, 1999; *Tomasko et al.*, 1999; *Lemmon et al.*, 2004). The small size of the dust grains pose as a hazard for particles to penetrate and damage exposed instruments, specifically moving mechanical parts. The atmospheric particles are also known to be electrostatically charged due to wind induced collisions with one another as a result of differences in sizes and contact potentials between the compositionally distinct materials (*Melnik and Parrot*, 1998; *Zhai et al.*, 2006). This resulting electrostatic charge has been attributed as being responsible for the adhesion of atmospheric dust onto the numerous landers and rovers dating back to the Mars Pathfinder's Sojourner (*Ferguson et al.*, 1999).

Alternative methods of dust adhesion have been observed through the magnetic properties of the Martian surface material. Experiments conducted by the Mars Pathfinder Lander (e.g. *Hviid et al.*, 1997) and the Mars Exploration Rovers (e.g. *Goetz et al.*, 2008) have identified the presence of magnetite in the martian dust that derives from mechanical weathering of the magnetite-rich surface rocks (*Bell*, 2008). The magnetic attraction further contributes to the adhesive properties of the suspended dust particles which, over time, settle out of the atmosphere and accumulate onto the various external instruments including cameras, communication antennas, and solar arrays; thus, creating hazardous situations for instrumentation that is required for numerous aspects of the daily operations for the vehicles.

Although the presence of the atmospheric dust poses many risks and challenges, it

does not hinder the drive to learn more about its abundance and interactions with the surrounding environment. At the time of this writing, there are five active spacecraft in orbit monitoring the Martian atmosphere. There have also been a number of landers and rovers sent to explore the Martian surface while also providing in situ measurements of atmospheric aerosols; most notably, using on-board imagers to measure extinction due to dust and ice in the atmosphere. These observations have been used for characterization of the local atmosphere as well as for providing ground truth sites for orbital observations of dust loading (*Lemmon et al.*, 2015).

1.4 Optical Depth

As radiation travels through an atmosphere, it has the potential to interact with aerosols and the atmospheric constituents. Optical depth is a dimensionless parameter that describes the amount of radiation that is attenuated through the processes of scattering and/or absorption as a beam of incident light passes through a layer of a planet's atmosphere. An optical depth value that is less than one indicates an atmosphere where very little incoming sunlight is attenuated; thus, in this case, most solar radiation is able to reach the planet's surface unobstructed. Optical depth values that are greater than one represent an atmosphere in which aerosols absorb and/or scatter the majority of incoming solar radiation, leaving minimal sunlight capable of reaching the surface.

Atmospheric optical depth is strongly influenced by the physical constitution as well as the concentration of localized aerosols; therefore, atmospheric circulation patterns play a significant role in determining optical depth values. For instance, coinciding with the previously discussed "dust storm season", high and variable opacities correlate with summer in the sourthern hemisphere (and perihelion) whereas generally low and stable opacities correlate with winter in the southern hemisphere (and aphelion) (*Lemmon et al.*, 2015). Although a common trend in regards to dust loading and local atmospheric opacity seems

to exist, the distribution of atmospheric dust can vary considerably throughout the course of a Martian year. This has been specifically attributed to the interannual variability that exists in Martian dust storm size, timing, and location of origin (*Mulholland et al.*, 2013).

Following the importance of dust on Mars being identified in *Gierasch and Goody* (1972), optical depth has been one of the key physical parameters used to quantify its presence and spatial distribution. Throughout the course of time, measurements of optical depth have been collected through numerous methods and various instrumentation aboard both landed and orbital spacecraft. Despite utilizing different platforms and approaches, the observations of optical depth serve the comprehensive purpose to provide insight on the Martian dust cycle; specifically focusing on climate and weather variability, thermal and dynamic atmospheric structure, and the transportation of aerosols and various chemical species (*Montabone et al.*, 2015)

1.4.1   Optical Depth Retrieval from Orbital Spacecraft

Orbital observations of the spatial and temporal variability of atmospheric dust aerosol opacity have been a focal point of every spacecraft mission sent to Mars dating back to the use of the infrared spectrometer aboard Mariner 9 that monitored the decay of the planet-encircling dust storm of 1971 (*Hanel et al.*, 1972). More recently, optical depth measurements of the total column have continued to be retrieved through missions such as the Mars Global Surveyor (MGS) (e.g. *Cantor et al.*, 2001; *Smith*, 2004; *Cantor*, 2007), Mars Odyssey (e.g. *Smith*, 2009), Mars Express (e.g. *Markiewicz et al.*, 2005; *Vincendon et al.*, 2007), the Mars Reconnaissance Orbiter (MRO) (e.g. *Wolff et al.*, 2009; *Heavens et al.*, 2011; *Hoekzema et al.*, 2011), and the Mars Orbiter Mission (MOM) (e.g. *Mishra et al.*, 2016). As of this writing, there exists a significant collection of heterogeneous, multiannual datasets of dust optical depth as they have been retrieved using various instruments that possess different observation geometries at specified wavelengths. Nevertheless, these

retrievals have been utilized in order to establish a climatology with near-global coverage (e.g. *Montabone et al.*, 2015) that is capable of analyzing both interseasonal and interannual variability of atmospheric dust opacity. While it is evident that orbital observations allow for a more complete characterization of dust optical depth over both spatial and temporal scales, they generally embody more modeling and/or retrieval assumptions in comparison to observations recorded from the surface. Essentially, orbital remote sensing observations lack the ability to provide the most desired measurement, a self-consistent "ground-truth"

1.4.2 Optical Depth Retrieval from Landed Spacecraft

Although the majority of the optical depth historical record is comprised of Earth-based and orbital remote sensing measurements, in situ data is of critical importance as it provides a higher level of accuracy and precision unattainable from the former (*Lemmon*, 2014). On Earth, the Aerosol Robotic Network (AERONET) exists and is a large organization of ground-based remote sensing aerosol systems established by the National Aeronautics and Space Administration (NASA), the PHysics, Optoelectronics, and Technology of Novel Micro-resonator Structures (PHOTONS), and expanded by other collaborators (*Dayou et al.*, 2014). In comparison, Mars has only possessed a handful of landers and rovers on the surface collecting aerosol data, two of which are currently active.

Generally, optical depth measurements observed from the surface of Mars have done so using direct solar imaging. These methods date back to the Viking lander missions (*Colburn et al.*, 1989) and have continued to be utilized through the use of the Pancam instrument on the Mars Exploration Rovers (MER) (*Lemmon et al.*, 2004, 2015), the Surface Stereo Imager on the Phoenix Mars Lander (*Lemmon*, 2010), as well as the Mastcam instrument aboard the Mars Science Laboratory (MSL) (*Lemmon*, 2014). The optical depth measurements that are derived from images of the solar disc are used to determine the

total optical depth in the column above the respective lander or rover. Although these methods of retrieval are well-established, an alternative technique has been performed as of recent utilizing the MSL's Navigation Cameras (Navcam) to measure the atmospheric optical depth along a line-of-sight for the lower portion of the Martian boundary layer.

In addition to assisting the navigation of the Martian terrain, the Curiosity rover's Navcams have been used to collect a series of Dust Devil Search Movies (DDSMs) in order to detect dust devil activity within Gale Crater. The images that are produced for the DDSMs can then be used to derive a line-of-sight extinction within the crater. In this procedure, Navcam radiometrically corrected images that are oriented due north capture visuals of the Martian sky, the distant crater rim, and the near ground. Three values are then extracted from the images: an average spectral radiance value for a patch of the sky, a patch from the mountains themselves, and a patch from the ground, respectively. *Moores et al.* (2015) and *Moore et al.* (2016) then used these derived values in a simplified radiative transfer analysis in order to discern how much optical depth exists between the observer (in this case the Curiosity rover) and a distant object (in this case the rim of the crater). Further details regarding the methodology behind the line-of-sight extinction calculations will be discussed in section 2.3.

Future missions to Mars that include landed spacecraft also possess the objective of monitoring atmospheric optical depth. The InSight lander mission, which is set to launch in May of 2018, possesses a pointable medium-resolution camera similar to the MER Navcam mounted at the end of a robotic arm. The Instrument Deployment Camera's (IDC) purpose was to capture black and white images of the deployed instruments and also provide a panoramic view of the Martian terrain surrounding the landing site. However, the IDC has since received an upgrade providing the camera with the capability to capture color sky images through the use of a red/green/blue (RGB) microfilter. This, in turn, will allow for an improved calculation of atmospheric line-of-sight dust opacity through the

9

recently established methods.

The Mars 2020 rover is another future mission that will possess the ability to measure optical depth in the Martian atmosphere as it will carry the Mastcam-Z camera system as well as possess a system of Enhanced Engineering Cameras (EECams) (*Bell et al.*, 2014; *Maki et al.*, 2016). Mastcam-Z derives heritage from the MSL Mastcam instrument, utilizing almost exact replicas of the device's electronics and sensors (*Gunn and Cousins*, 2016). The Mastcam-Z imager will be able to acquire visible color (RGB), stereo panoramas of the Martian surface as well as direct images of the sun through the use of a pair of solar filters; thus, permitting the use of similar techniques previously used for MER and MSL imaging in order to produce measurements of atmospheric column optical depth. The EECams incorporate proven heritage design principals from the MER and MSL Navcams and Hazcams. Both camera types will possess the capability to produce color images and will be a significant improvement from their previous generation counterparts as they will have more resolving power and provide a wider field of view (FOV). Measurements of line-of-sight optical depth will be able to be observed similarly to the MSL through Navcam images that utilize the radiative transfer image analysis established in *Moores et al.* (2015) and *Moore et al.* (2016); thus, providing further contribution to the ever growing record of Martian optical depth observations.

1.5 Research Objectives

The simplified radiative transfer image analysis possesses significant assumptions that are required in order to drive the model. Through the use of various assumptions initially established in *Moores et al.* (2015), the majority of the radiative transfer processes that occur within the Martian atmosphere are disregarded, particularly pertaining to the contributions of the source function. Furthermore, the assumptions that are applied remove not only the three-dimensionality of the atmosphere, but the one-dimensionality as well

through the attribution that the Martian atmosphere possesses a singular source function over all angles of observation. Despite the use of such substantial assumptions, the results produced through this radiative transfer analysis have been utilized to address questions essential to understanding the environment surrounding the MSL (e.g. whether Gale Crater is a source or a sink of atmospheric dust in its current era).

In order to assure that landed spacecraft for both present and future operations possess the robust capability of determining line-of-sight atmospheric optical depth, a three-dimensional radiative transfer model has been developed to produce simulated atmospheric data that enables the simplified methodology for measuring dust content presented in *Moores et al.* (2015) and *Moore et al.* (2016) to be evaluated and validated while limiting the number of required free parameters. In this model, the radiative transfer equation (RTE) was integrated over a line-of-sight in an arbitrary atmosphere that is a set of spherical shells and is horizontally homogeneous except for the existence of an idealized crater with allowed in-crater versus out-of-crater differences. This thesis seeks to test the simplified method under a variety of geometries and over the range of relevant wavelengths in order to identify the existence of specified limitations that could alter and/or further develop the previously established observations within Gale Crater.

Chapter two will discuss the MSL and the instruments utilized for optical depth observations, detail how the retrievals are made, and address the provided datasets. Chapter three will focus on the methods used in the three-dimensional modeling of radiative transfer. More specifically, chapter three will address the reading and input of data into the model, detail the methods behind the contributions from both single and multiple-scattering sources, and discuss what is output from the radiative transfer model. Chapter four addresses and discusses the results produced through the numerous runs of the model, particularly focusing on the limitations that are exhibited. The final chapter provides the conclusions of the work, detailing the limitations of the simplified methods of radiative

transfer and suggestions for future improvements.

2. DATA AND OBSERVATIONS

2.1 Overview

Preceding the arrival of the Curiosity rover, an extensive atmospheric modeling program was conducted in order to examine the atmospheric circulations within Gale Crater. The primary objective of this investigation was to better understand the influence of possible atmospheric and environmental interactions that would pose a hazard throughout the lower portion of the EDL phase for the spacecraft (*Vasavada et al.*, 2012). Along with offering a broad description of the circulation within the crater itself, this study also produced results that projected for a suppression of the thickness of the planetary boundary layer (PBL) that ranged from 1 to 2 km within the crater in comparison to 8 to 10 km outside of the crater (*Tyler and Barnes*, 2013). Consequently, a suppressed PBL would reduce the strength of convective mixing which would result in the production of fewer and/or less intense dust devils in comparison to other similar locations on Mars (*Kahanpää et al.*, 2013; *Moores et al.*, 2015; *Kahanpää et al.*, 2016). Furthermore, the suppressed PBL would also reduce the dust loading of the near-surface atmosphere in comparison to the air above the crater (*Moore et al.*, 2016). In order to observe the implication of the relatively minuscule intra-crater mixing ratio of dust, both the Mastcam and Navcam instruments aboard the MSL were employed.

2.2 The Mastcam Instrument and Observations of Optical Depth

The Mastcam consists of two color cameras mounted approximately two meters above the surface on the Curiosity rover's Remote Sensing Mast (RSM). Each of the camera heads has the ability to mechanically focus as well as autofocus (*Malin et al.*, 2005). Furthermore, the individual cameras possess different focal lengths and science filters which broaden the scientific capabilities of the Mastcam imagers. The instrument acquires im-

ages of up to 1200 lines by 1648 samples (1200 by 1608 photoactive pixels) with the ability to capture consecutive images at a uniform frame rate. The cameras acquire color from the use of Bayer-pattern filters on the Charged Coupled Device (CCD), similar to consumer digital cameras, but also possess selectable science filters that image through the Bayer-pattern filters (*Malin et al.*, 2013). For a more detailed description of the Mastcam imagers and optics, see *Malin et al.* (2013).

Each Mastcam camera head also possesses an 8-position filter wheel; therefore, allowing for images to be captured while looking through a range of various wavelengths. One of the positions in each camera is a broadband infrared cutoff filter for use with the Bayer color capability of the CCD. Twelve of the sixteen filter positions provide color-imaging capability at wavelengths ranging from 400 to 1100 nm of which three filters are shared by the individual cameras. Lastly, two filters (one on each camera at wavelengths of 440 and 880 nm) with neutral density coatings provide the cameras with the ability to capture direct images of the sun from the Martian surface (*Malin et al.*, 2013).

Solar-imaging sequences from the Mastcam instrument possess three variations in which they image the sun in each filter, they image the sun in each filter and capture the sky near the sun, or they capture video of the sun in order to observe transits of the Martian moons (*Lemmon*, 2014). Although various observation methods exist, measurements of atmospheric optical depth are developed through the use of direct solar imaging. Following the capture of the direct solar images, the pictures are initially downlinked to Earth as thumbnail images. Within these images, the Sun measures 10 pixels in diameter at 440 nm (Mastcam 100 mm focal length camera) and 3.3 pixels in diameter at 880 nm (Mastcam 34 mm focal length camera). For each pixel in the raw captured image, the data were converted to 8 bits through the use of an onboard look-up table. Depending on operational circumstances, the images are either downlinked with lossless compression or with JPEG quality 95 compression. Once downlinked, the images were converted back to

14

12 bits. Furthermore, various corrections were applied which included correction for electronic bias, dark current, and any scattered light background. Following this, the images were exposure time and flat-field corrected which, in turn, produced images with radiances expressed in effective data numbers (DN) per second (*Lemmon*, 2014).

Conversion of the direct solar images into measurements of atmospheric optical depth is fundamentally simple as optical depth can be derived through the use of the Beer-Lambert-Bouger extinction law, $F = F_{TOA}e^{-\tau\eta}$. In this equation, F is the observed solar flux, F_{TOA} is the direct solar flux at the top of the atmosphere, τ is the normal optical depth, and η is the airmass which is defined as the ratio of the optical depth along an arbitrary line-of-sight to the normal optical depth in the zenith direction. Equivalently, η can be approximated as the secant of the solar zenith angle for plane-parallel, homogeneous atmospheres (*Lemmon*, 2014; *Lemmon et al.*, 2015). For further details regarding this process, refer to *Lemmon et al.* (2015).

Mastcam optical depth sequences began on sol 33 and have continued to nominally be retrieved every three to seven sols. In comparison to the Spirit and Opportunity rovers, daily measurements are not required for monitoring the Curiosity rover; thus, optical depth observations only occur when they are specifically inserted into the daily rover operations in order to not take away resources from other objectives. Despite the lack of daily measurements, much of the overall description of the annual cycle of aerosol optical depth at Gale Crater can be interpreted from the Mastcam observations (*Smith et al.*, 2016). It is for this reason that this thesis utilizes two datasets consisting of Mastcam optical depth observations provided by Mark Lemmon.

The initial dataset provided consisted of 1340 Mastcam column optical depth measurements representing the observations from sol 1 through sol 1340 which far exceeded the number of sols analyzed in *Moores et al.* (2015) and *Moore et al.* (2016). The Mastcam measurements utilized in this dataset were interpolated between observations in order to

provide a continuous, simulated seasonal record of column opacity. The second dataset provided was to act as a surrogate to the data utilized in *Moores et al.* (2015) and *Moore et al.* (2016). The dataset consisted of 497 Mastcam column optical depth measurements observed by the left-mounted 34 mm focal length camera using the 880 nm neutral density filter. The observations spanned from sol 33 to sol 1476, similarly exceeding the observed sols in the publications. Furthermore, certain sols in the dataset were seen to possess more than one measurement which is attributed to the common occurrence of an instrument calibration.

2.3   The Navcam Instrument and Observations of Optical Depth

As briefly mentioned in section 1.4.2, an alternative method to direct solar imaging for atmospheric optical depth observations has been developed and performed as of recent through the use of the MSL's Navcams (*Moores et al.*, 2015; *Moore et al.*, 2016). The navigation camera system consists of four imagers mounted on the Curiosity rover's RSM. The MSL Navcams are build-to-print copies of the MER cameras which are described in detail in *Maki et al.* (2003). There are two left-right pairs of Navcams aboard the MSL in which the individual pairs are connected to a separate computer system within the rover body. One pair is used for stereoscopic imaging while the other pair serves as a backup. The Navcam imagers possess 1024 by 1024 pixel CCD detectors with a nearly square 45-degree FOV. The Navcam is capable of achieving a signal-to-noise ratio better than 200:1 for well-exposed images. Furthermore, the Navcam imagers are broadband filtered such that their response spans the range of 600 to 850 nm. For a complete description of the instrumentation and technical specifications of the Navcam imagers produced for MSL, see *Maki et al.* (2012).

Although the main objective of the Navcams aboard the MSL was to provide terrain context of the Martian surface for traverse planning and Mastcam/Chemcam pointing,

the instrument has proven to be particularly versatile through its collection of DDSMs in order to detect dust devil activity within Gale Crater (*Moores et al.*, 2015). Using the observations acquired from the dust devil searches, it is possible to derive a time series of line-of-sight optical depth measurements within the crater that complement the Mastcam column optical depth measurements. As discussed in the previous section, Mastcam optical depth observations describe the total optical depth within a vertical column of the Martian atmosphere directly above the Curiosity rover and are insensitive to the vertical distribution of dust. Conversely, line-of-sight measurements provide information on the dust optical depth within the crater itself (the bottom 2 to 3 km of the atmosphere); therefore, allowing for the vertical distribution of dust to be separated into two distinct regions, 'above' the crater and 'in' the crater (*Moores et al.*, 2015). These observations can then be used to identify where the majority of the dust observed in the Mastcam optical depth measurements is allocated.

The DDSM observations established in *Moores et al.* (2015) are collected when the Navcam is oriented due north, capturing visuals that display the near ground, the Martian sky, and the distant crater rim. In order to calculate the optical depth along a line of sight, three values must be extracted from the visuals presented in the radiometrically corrected images: an average spectral radiance value from a patch of the ground near the rover, an average spectral radiance value for a patch of the Martian sky, and an average spectral radiance value from a patch of the mountains themselves. The radiance of the ground near the rover, I_G, is obtained by selecting a patch of the Martian surface that contains both completely sunlit and shadowed regions and averaging the observed radiance over all of the pixels within the patch.

The first assumption for retrieving the radiance of the near-ground is that the material that defines the Martian ground is comparable to the material that the mountains are comprised of as supported from orbital measurements of albedo (*Putzig and Mellon*, 2007).

17

The second assumption holds that the reflectance of the surface material is sufficiently Lambertian, meaning that regardless of an observer's angle of view, the surface possesses the same apparent brightness. This assumption allows for the phase function of the ground to vary little at the observation angles of the ground and the mountains that differ on the order of a few degrees for the relatively gentle slopes of the crater rim. A third assumption from *Moores et al.* (2015) holds that the optical depth that exists between the Navcam and the ground itself can be considered negligible as the rover is at a distance of a few tens of meters from the observation location; thus, the measurement of radiance of the nearby ground can be used as a proxy for the radiance of the mountains, I_M, if the optical depth between the Navcam and the mountains were zero.

$$I_M(\tau = 0) \approx I_G \tag{2.1}$$

Following the retrieval of the ground radiance, the radiance of the sky, I_S, may be observed directly if a path just above the crater rim mountaintops is selected (using an elevation angle of approximately three degrees). The observed sky radiance can then be further utilized to calculate the radiance value representative of scattering by the presence of atmospheric dust aerosols. In order to obtain information from the brightness of the sky to which the brightness of the dust within the crater may be compared, assumptions are made to substantially simplify the complex expressions. The initial assumption for these calculations establishes that, along a single path, the particles being considered are of the same size and of the same composition; thus, their phase functions, *P*, will be equivalent.

Furthermore, the conditions under which the atmospheric dust particles are illuminated across the crater floor and along a nearly horizontal path above the crater are likely to be substantially similar; therefore, the radiation incident on the dust particles from an

arbitrary direction should be equivalent for both the dust and sky cases. Through this assumption, it holds that the source function, J_D, will also be equivalent for both cases. Lastly, it is assumed that a constant single scattering albedo, $\tilde{\omega}$, exists over the 650-800 nm wavelength range. Following the implementation of the assumptions, various equations were derived in *Moores et al.* (2015) through definitions established in *Hansen and Travis* (1974) in order to address the radiative contribution of the scattered dust. Further analysis of these equations, in conjunction with typical column optical depths observed by Mastcam, also lead to the revelation that the total optical depth along the considered path (τ_0) may be assumed to be infinite and the radiance of the Martian sky may be defined as $I_S = \tilde{\omega} J_D$.

Similar to the prior retrievals, the average spectral radiance of the mountains, I_M, is observed directly by averaging over the pixels within a patch of the mountains. The optical depth between the mountains and the Navcam can then be determined by assuming that the radiance of the mountains as viewed through a long path length of atmosphere with an unknown optical depth, $I_M(\tau_0)$, may be expressed as the sum of the radiance of the mountains at optical depth zero, $I_M(\tau = 0)$, which is approximately equal to the radiance of the ground per equation 2.1, and the contributed radiance of the Martian dust.

$$I_M(\tau_0) = I_G exp(-\tau_0) + \tilde{\omega} J_D [1 - exp(-\tau_0)] \qquad (2.2)$$

Provided that the angle of viewing geometry of the dust for the sky just above the crater rim mountaintops and just below the crater rim varies by approximately one or two degrees at most, it is assumed that the phase function, *P*, for both individual paths is equivalent; thus, the values of the source function are also equivalent. Through these assumptions and prior established assumptions of a constant single scattering albedo as well as the

optical path above the mountains being effectively infinite, the following relationship may be derived:

$$\tilde{\omega} J_{D_{mountains}} = \tilde{\omega} J_{D_{sky}} = I_S \tag{2.3}$$

Substitution of this relationship can then be applied into equation 2.2 which produces

$$I_M(\tau) = I_G exp(-\tau) + I_S[1 - exp(-\tau)] \tag{2.4}$$

Equation 2.4 can then be rearranged in order to solve for the unknown optical depth between the Navcam and the crater rim mountains; thus, producing the principal equation that is utilized for the simplified radiative transfer image analysis in *Moores et al.* (2015) and *Moore et al.* (2016).

$$\tau = -ln\left[\frac{I_M - I_S}{I_G - I_S}\right] \tag{2.5}$$

Through the derivation of the fundamental equations, the simplified radiative transfer model seems to be well-supported and on solid ground; however, the methods possess weakness within a few of the assumptions. For instance, regardless of the optical depth between the observer and the crater rim mountains, the surface itself does not see the same sky at the crater rim as in the near field. Furthermore, through the assumptions taken for the Martian sky, a significant portion of the atmospheric radiative transfer processes are disregarded, specifically pertaining to the contributions of the source function. Similar assumptions are carried out in producing the final equation which display that the source function is constant regardless of viewing path geometry. However, under no circumstance is the source function amongst the ground, sky, and sun static from space to the surface of the planet. It is due to the nature of these assumptions being substantial that this thesis tests the simplified methods of radiative transfer presented in *Moores et al.* (2015) and

Moore et al. (2016).

3. METHODS

3.1 The Radiative Transfer Equation

In order for optical depth to be retrieved, a definition of the radiative transfer equation (RTE) must first be established. As a beam of solar radiation propagates through an atmosphere, it is influenced by the processes of absorption, emission, and scattering. The three individual processes govern the quantity of energy that the beam possesses such that it loses energy to absorption, gains energy through emission, and redistributes energy through scattering (*Möller*, 2014). These atmospheric interactions are mathematically defined through the RTE. A concise version of the standard form of the 1-dimensional RTE for diffuse radiance can be seen in equation 3.1.

$$\mu \frac{dI_{diff,\lambda}(\tau,\mu,\varphi)}{d\tau} = I_{diff,\lambda}(\tau,\mu,\varphi) - J_{total}(\tau,\mu,\varphi) \tag{3.1}$$

The RTE above is an integro-differential equation for the diffuse spectral radiance $I_{diff,\lambda}$ as it contains both a differential and an integral term. The equation is also known as the Schwarzchild-Emden differential equation and represents a general radiative transfer equation for a horizontally homogeneous atmosphere with plane-parallel geometry (*Wendisch and Yang*, 2012). On the left-hand side of equation 3.1 is a differential that describes the rate at which the diffuse spectral radiance (dependent on τ optical thickness, μ the cosine of the polar angle, and φ the azimuth angle) varies with optical thickness. The right-hand side of the equation consists of the difference between the total diffuse spectral radiance and the total source function. In the absence of thermal emission, attributed to modeling radiative transfer in the visible and near-infrared wavelength range, the total source function, J_{total}, can be decomposed into two individual parts being direct and dif-

fuse (*Mendrok*, 2006). The two terms within the source function are displayed in equation 3.2 and to a more elaborate extent in equation 3.3.

$$J_{total} = J_{dir,\lambda} + J_{diff,\lambda} \tag{3.2}$$

$$
\begin{aligned}
J_{total} = \\
\tilde{\omega}(\lambda, \tau) * S_{dir,\lambda,TOA} * e^{-\tau/\mu_0} * \frac{P(\lambda, \tau, -\mu_0, \varphi_0, \mu, \varphi)}{4\pi} \\
+ \tilde{\omega}(\lambda, \tau) \int_0^{2\pi} \int_{-1}^1 I_{diff,\lambda}(\tau, \mu^{'}, \varphi^{'}) * \frac{P(\lambda, \tau, \mu^{'}, \varphi^{'}, \mu, \varphi)}{4\pi} d\mu^{'} d\varphi^{'}
\end{aligned}
\tag{3.3}
$$

The first source term on the right-hand side is representative of the first-order scattering of direct solar radiation in the direction (μ, φ). The incident solar radiation, $S_{dir,\lambda,TOA}$, at the top of the atmosphere (TOA) is exponentially attenuated according to the Beer-Lambert-Bouguer extinction law until it is scattered into the direction (μ, φ) enhancing $I_{diff,\lambda}(\tau, \mu, \varphi)$. The scattered portion is quantified by the phase function, *P*, and the absorption is determined by the single scattering albedo, $\tilde{\omega}$ (*Wendisch and Yang*, 2012). The second source term represents multiple scattering by the entire atmosphere. This term includes the diffuse radiances scattered into the direction (μ, φ). Therefore, the incoming diffuse radiances are multiplied by the phase function and integrated over the solid angle with the single scattering albedo determining how much of the diffuse radiance is scattered in the extinction process (*Wendisch and Yang*, 2012). In this work, the first-order scattering contribution to the RTE will be calculated analytically; however, the calculation of the multiple-scattering contribution is more complex.

3.2 Discrete-Ordinate-Method for Radiative Transfer (DISORT)

Located within both the single-scattering and multiple-scattering components of the source function is the phase function. The phase function is defined as a non-dimensional parameter used to characterize the angular distribution pattern of radiation scattered by a particle at a given wavelength. Scattering particles within the Martian atmosphere possess mean radii that are either comparable or exceed the wavelengths of the incoming the solar radiation (e.g. *Kuhn and Atreya*, 1979); thus, causing the scattering to become extremely forward-peaked (*Pierrehumbert*, 2010). This in turn produces strongly asymmetric phase functions that are notorious for causing significant difficulties in performing calculations of the RTE. More specifically, solutions become very computationally intensive to retrieve (*Wiscombe*, 1977). In order to avoid the unnecessary processing complications, the multiple-scattering contribution of the source term was calculated through numerous runs of the Discrete-Ordinate-Method Radiative Transfer (DISORT) numerical algorithm which characterized the diffuse radiation field as a function along the arbitrary Navcam line-of-sight. DISORT is a general-purpose Fortran program used to model the transfer of monochromatic, unpolarized radiation from one location to another by absorbing, emitting, and scattering in a vertically inhomogeneous, plane-parallel medium that successively produces intensities at user-selected angles and levels as the common output (*Stamnes et al.*, 2000).

Generally, strongly forward-peaked phase functions and scattering in the Mie regime incites significant difficulty; however, DISORT utilizes the "δ - M method" to ensure accurate and efficient computational calculations (e.g. *Wiscombe*, 1977). Furthermore, the δ - M method has proven to be a very useful truncation procedure for flux computations as it captures the kind of anisotropy (strong forward peak due to diffraction) found in almost all natural scattering phenomena. The essence of the δ - M method is to separate the phase

function, *P*, into the sum of a delta-function in the forward direction and a truncated phase function, *P'*, which is expanded in a series of Legendre polynomials (*Stamnes et al.*, 2000). In order to reconstruct the phase function to best represent the Martian atmospheric dust particles, a total of 256 Legendre polynomial moments are utilized which are represented by M in the following equation:

$$P(\tau, cos(\theta)) = \sum_{l=0}^{2M-1} (2l+1)g_l(\tau)P_l(cos(\theta)) \tag{3.4}$$

where the expansion coefficients, by virtue of the orthogonality of the Legendre polynomials, are given by

$$g_l(\tau) = \frac{1}{2} \int_{-1}^{+1} P_l(cos(\theta))P(\tau, cos(\theta))d(cos(\theta)) \tag{3.5}$$

In DISORT, the phase function is assumed to depend solely on the angle between the incident and scattered beams, θ, as opposed to the incident and scattered directions individually. This assumption, in conjunction with the expansion of the phase function into a series of Legendre polynomials (e.g. equation 3.4), can then be utilized in order to separate the azimuthal-dependence in both equation 3.1 and equation 3.3. To finalize the factoring out of the azimuthal-dependence, the measured intensity is then expanded into a Fourier cosine series:

$$I(\tau, \mu, \varphi) = \sum_{m=0}^{2M-1} I^m(\tau, \mu)cos(m(\varphi_0 - \varphi)) \tag{3.6}$$

Substitution of equations 3.4 and 3.6 into the original RTE (equation 3.1) in turn causes for equation 3.1 to separate into 2*M* independent integro-differential equations (one for

each azimuthal intensity component) which produces the following equation:

$$\mu\frac{dI^m(\tau,\mu)}{d\tau} = I^m(\tau,\mu) - J^m(\tau,\mu) \quad (m = 0, 1, 2M - 1) \tag{3.7}$$

The discrete ordinate approximation for the above equation can be obtained by approximating the integral within the source function by a quadrature sum; therefore, transforming the above integro-differential equation into the following system of differential equations where M represents the number of Legendre polynomial moments and N represents the total number of quadrature angles or "streams" utilized for the upward-looking geometry. In order to represent the angular distribution of both atmospheric and surface scattering on Mars, a total of 64 streams and 256 Legendre polynomial moments (M) were used in the following equation:

$$\mu_i\frac{dI^m(\tau,\mu_i)}{d\tau} = I^m(\tau,\mu_i) - J^m(\tau,\mu_i) \quad (m = 0, 1, 2M - 1) \quad (i = \pm 1, \pm N) \tag{3.8}$$

The integrated solution to equation 3.8 produces the measured intensity of the diffuse radiation field along a specified line of sight at any point in the atmosphere from the arbitrary location of an "observer" on the surface. However, this solution is produced under the DISORT assumptions of a plane-parallel, horizontally homogeneous atmosphere, whereas the three-dimensional radiative transfer model for this work possesses horizontal inhomogeneity.

3.3 Radiative Transfer in a Horizontally Inhomogeneous Environment

The environment of Gale Crater itself is responsible for in-crater versus out-of-crater atmospheric differences; therefore, the three-dimensional radiative transfer model will integrate the RTE in a non-horizontally homogeneous atmosphere by using an analyti-
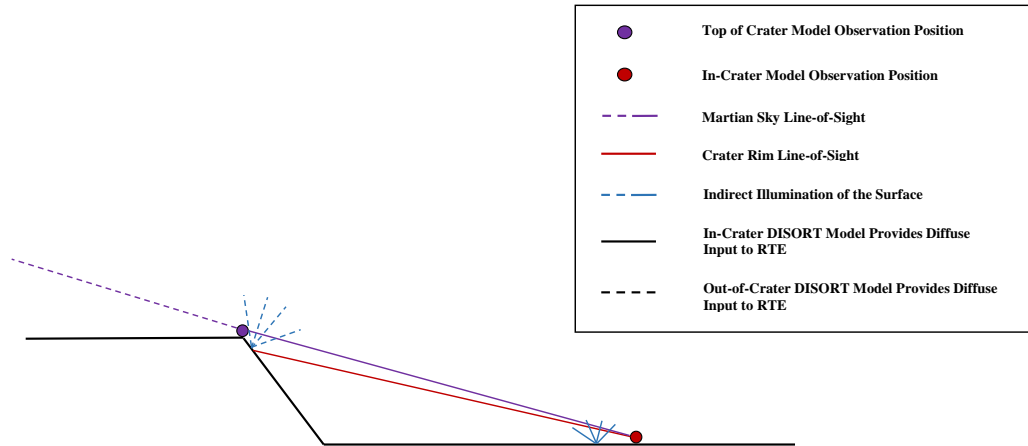
Figure 3.1: Visual representation of the observer locations and relative observational lines-of-sight representative of the DISORT 3-dimensional radiative transfer model parameter retrieval within the Gale Crater environment.

cal calculation for the single-scattering contribution and DISORT to solve for the source function of the multiply scattered light. The key approximation for the model is that the plane-parallel, horizontally homogeneous results are used under the non-plane-parallel and horizontally inhomogeneous circumstances. Through this approximation, the model is able to calculate the variability of the source function with high fidelity in comparison to the simplified methods used in *Moores et al.* (2015) and *Moore et al.* (2016) that utilize a singular, static source function.

The three-dimensional radiative transfer model in this work encompasses two individual runs that produce five desired measurements of intensity necessary to represent the radiative transfer processes that occur within the Gale Crater environment on Mars. A visual representation of the individual model observations can be seen in Figure 3.1. The initial model run sets the location of the observer at the top of the Gale Crater rim which is approximately 2 km above the designated surface of Gale Crater (indicated by the purple

circle in Figure 3.1). In this run, the observer is looking outward from the crater and the RTE is integrated over the observer's line-of-sight in DISORT (indicated by the dashed purple line in Figure 3.1).

In the second model run, the radiative transfer within Gale Crater is represented as the location of the observer is set on the defined crater surface to represent the MSL Curiosity rover (indicated by the red circle in Figure 3.1). As opposed to the singular line-of-sight observation in the initial model run, the second run possesses two individual lines of sight in which the RTE is integrated over. The two lines of sight correspond in position to those utilized in *Moores et al.* (2015) and *Moore et al.* (2016) such that one of the observations lies above the mountains and the other purposefully clips the edge of the crater rim as illustrated by the solid purple and solid red line in Figure 3.1, respectively. Furthermore, the observation from the surface along the line-of-sight directed at the Martian sky is truncated at the crater rim elevation; therefore, bisecting the individual model runs into two distinct layers being "above" the crater and "within" the crater.

In order to extract the three principal radiance values addressed in *Moores et al.* (2015) and *Moore et al.* (2016), the three-dimensional radiative transfer model is ran, first using DISORT to integrate the RTE over the line-of-sight of the sky from the top of the crater. This in turn retrieves the intensity of the Martian sky in terms of the integral of the source function along the line-of-sight:

$$I'_S = \int J_{total_{TOC}}(s)ds \tag{3.9}$$

For the second model run, DISORT similarly integrates the RTE over the line-of-sight of the Martian sky from the surface to the crater rim altitude; thus, producing a measurement of intensity in terms of the integral of source function along the specified line-of-

sight. However, in order to extract the total intensity measured encompassing both of the bisected regions, the calculated value of intensity of the Martian sky observed from the top of the crater is used as the diffuse spectral radiance in the discrete ordinate approximation for the RTE. This value is exponentially attenuated by the user-supplied atmospheric optical depth within the crater and is then added to the intensity derived in the second model run. Therefore, producing one of the three principal radiance values from *Moores et al.* (2015) and *Moore et al.* (2016) as displayed in the following equation:

$$I_S = I'_S \, e^{\tau_s} + \int J_{total_{Sfc-Sky}}(s)ds \qquad (3.10)$$

Next, the spectral radiance of the crater rim mountains can be derived by once again using a combination of the first and second model runs. In the initial model run, the direct illumination of the crater rim mountains themselves, I_{crt}, was derived as the integration of the diffuse light incident on the Martian surface in addition to the direct solar contribution with the total flux divided by π converting it to a radiance value (indicated by the dashed blue lines in Figure 3.1). Through the second model run, DISORT integrates the RTE over the line-of-sight from the arbitrary observer location on the surface to the crater rim mountains producing an intensity in terms of the integral of the source function along the line-of-sight (illustrated as the solid red line in Figure 3.1). Similar to the Martian sky radiance retrieval, the value derived in the initial model acts as the diffuse spectral radiance in the discrete ordinate approximation for the RTE and is attenuated exponentially by the user-supplied value of atmospheric optical depth; thus, providing the following equation for the spectral radiance of the crater rim mountains:

$$I_M = I_{crt} \, e^{\tau_s} + \int J_{total_{Sfc-Crt}}(s)ds \qquad (3.11)$$

Finally, the spectral radiance of the surface near the Curiosity rover is calculated through the use of the second model run. Similar to the observation of the illumination of the tilted crater rim surface, the illumination of the surface near the rover is derived through the integration of the diffuse light incident on the Martian surface in addition to the source of direct solar contribution. This value is then divided by π in order to convert the flux into a radiance value producing the following equation:

$$I_G = \frac{I_{dir,sfc} + \int I_{diff,sfc}}{\pi} \qquad (3.12)$$

Following the derivation of the radiance of the surface near the rover, all three of the principal radiance measurements for the simplified analysis of the radiative transfer equation from *Moores et al.* (2015) and *Moore et al.* (2016) have been established. However, through the use of the three-dimensional radiative transfer model, the substantial assumptions that lead to the static source function in the Martian atmosphere have been removed; thus, displaying the resourcefulness and versatility of DISORT in modeling the computationally intensive multiple scattering regime of the RTE for this three-dimensional model of the Martian atmosphere.

3.4 Simulating the Navcam Measurements

In order for three-dimensional radiative transfer analysis to successfully model the Martian atmosphere and simulate the observations from the Navcam instrument to test the assumptions regarding the source function and surface originally established in *Moores et al.* (2015), a program written using Interactive Data Language (IDL) was developed to drive the model. The objective of this program was to provide DISORT with the numerous user-supplied input parameters similar to the two publications that were necessary for the intensive computations of the source function and following radiance values. The collec-

tion of user-supplied parameters were read into the program through the use of an IDL input structure. As briefly discussed in section 2.2, two datasets were provided by Mark Lemmon consisting a time series of Mastcam column optical depth measurements; however, both datasets also possessed a collection of other variables relative to the Mastcam observations.

In addition to the optical depth observations, the initial dataset consisted of 1340 Martian relative time references as well as the solar geometry. The time reference is provided in both Martian sol and well as solar longitude, the Mars-Sun angle measured from the northern hemisphere spring equinox where $L_s = 0$. The solar geometric angles provided are the solar elevation angle and the solar azimuth angle recorded when the sun was at its peak. The variables in the presented surrogate dataset were similar to those supplied by the initial dataset; however, the values within this dataset were more specified to the Mastcam observations. For instance, Martian sol was expressed as a decimal sol which is defined as the addition of the sol number with the local true solar time (LTST) divided by 24. The solar longitude as well as the solar geometric angles are also specified to these time relative measurements.

Within the input structure, the solar geometry is read in from the datasets with the solar elevation angle, μ_0, and the solar azimuth angle, ϕ_0, values being converted from degrees to radians. Following this, the Mastcam optical depth which represents the total optical depth above the Curiosity rover is read in from the provided datasets and is noted as τ_{MSL}. In order to allocate the variance between how much optical depth is within the crater (below the crater rim mountaintop altitude of 2 km) and how much optical depth is above the crater, the Martian atmosphere is assumed to be well-mixed such that the dust-mixing ratio is constant with height. This assumption allows for the optical depth above the crater, τ_{crater}, to be solved for using the following basic equation where z represents the crater rim altitude and H represents the scale height of the Martian atmosphere which

is approximated as 10.7 km for carbon dioxide at 210 K (*Moores et al.*, 2015):

$$\tau_{crater} = \tau_{MSL} - \tau_{MSL}(1 - e^{-z/H}) \tag{3.13}$$

From this calculation, the atmospheric optical depth outside of the crater, τ_{out} could then be assessed as it was assumed to be equivalent to τ_{crater} for the default case utilized in this work. Furthermore, through the use of equation 3.13, various cases in which the atmospheric aerosol opacity was assumed to be depleted and/or enhanced within the crater were produced simply by multiplying the secondary τ_{MSL} by the desired fraction of depletion and/or enhancement.

In order to coincide with the observations from *Moores et al.* (2015) and *Moore et al.* (2016), the established observation geometry input parameters were to be kept consistent; therefore, the observation elevation angle of the Martian sky, μ_{top}, was set to three degrees. Furthermore, the observation elevation angle that intersects the crater rim, μ_{bottom} was set to two degrees as the viewing geometry between the sky and crater rim differed by approximately 1 degree (*Moores et al.*, 2015). To address the geographic inhomogeneity of the line-of-sight extinction observations, the observation azimuth (ϕ_1) input parameters were loosely based on the five individual regions along the crater rim analyzed in *Moore et al.* (2016) which allowed for a better comprehension of the variability across the 45-degree wide Navcam frame. In the established work, the captured images took the center of the image to be due north or an observation angle of $0°$. The following four observations were made at both $9.6°$ and $19.2°$ east and west of due north.

This work elected to keep the spacing of the observation azimuth at $9.6°$ while further expanding the observation frame out to $48°$; therefore, this analysis made use of the six following observation azimuth angles: $0°, 9.6°, 19.2°, 28.8°, 38.4°$, and $48°$. Al-

though the maximum user-supplied observation azimuth exceeds the frame capabilities of the Navcam, the extension of the observation azimuth allows for a deeper analysis of the geographic inhomogeneity experienced in these measurements while keeping it relatively close to the original observations in *Moore et al.* (2016). Furthermore, the extension to $48°$ in the three-dimensional model was also prompted by the fact the performing an east to west analysis as done in *Moore et al.* (2016) would yield symmetric values; thus, substantially limiting the inhomogeneity analysis.

The final set of parameters necessary to run DISORT consisted of the albedo of the Martian surface (ω_{sfc}), the single scattering albedo (SSA) of the Martian dust particles ($\tilde{\omega}$), and the phase function representative of the Martian dust. For this work, the albedo of the Martian surface was kept at a constant in which $\omega_{sfc} = 0.225$. The SSA and phase functions parameters were provided in a set of four text files where each file represented a different filter. One file provided was specific to the MSL Navcam whereas the other three files consisted of the SSA and phase functions for the red (640 ± 44 nm), green (544 ± 38 nm), and blue (495 ± 37 nm) L0 filters for the 34 mm left-mounted Mastcam. For all four files, the imaginary index was varied in order to produce a SSA that approximately corresponded to the values observed in *Wolff et al.* (2009). Furthermore, the phase functions were based upon the dust particle properties observed at the Mars Pathfinder landing site as discussed in *Tomasko et al.* (1999) and *Johnson et al.* (2003).

Following the reading in of all of the various parameters through the input structure, the three-dimensional model is ran, subsequently deriving the three principal values of radiance (I_G, I_S, and I_M) produced in equations 3.10, 3.11, and 3.12. The derived radiance values are then plugged into equation 2.5 to simulate the Navcam measurements in the established publications and solve for the line-of-sight optical depth within Gale Crater between the Curiosity rover and the distant crater rim. For comparison of the results from the three-dimensional radiative transfer model to those reported in *Moores et al.*

(2015) and *Moore et al.* (2016), the values of optical depth produced are then converted into extinction for through division of the optical depth values by the distance from the Curiosity rover to the crater rim. The distance from the rover to the crater rim was analytically solved for using the viewing geometry and the crater altitude; therefore, allowing this work to produce a variety of time series plots of line-of-sight extinction within Gale Crater possessing numerous cases that include instances of in-crater depletion and enhancement and various observation geometries. The results from this work can then be compared to those produced in *Moores et al.* (2015) and *Moore et al.* (2016), providing the ability to search for the existence of specified limitations that could alter and/or further develop the previously established observations within Gale Crater.

4. RESULTS AND DISCUSSION

4.1 Seasonal Variation of Line-of-Sight Extinction

The environment within Gale Crater was found through various studies to be a dynamically stable and relatively inactive region for dust lifting activity which has been attributed to the presence of a suppressed PBL that inhibits the strength of convective mixing (e.g. *Kahanpää et al.*, 2013; *Moores et al.*, 2015; *Kahanpää et al.*, 2016) and reduces the quantity of dust loading in the near-surface atmosphere in comparison to the air aloft (*Moore et al.*, 2016). The reduction of dust and creation of a relatively dust-free zone near the surface is further driven by the mechanics of atmospheric circulations within the northern portion of Gale Crater (e.g. *Tyler and Barnes*, 2013) that substantially restrict mixing with the air outside of the crater. Although mixing between the bisected regions "above" and "within" the crater is commonly held to a minimum, *Moores et al.* (2015) exhibited an instance following the occurrence of an out-of-crater dust event near sol 100 in which the Mastcam column extinction and the line-of-sight extinction reacted through conspicuous increases in value; thus, presenting behavior that suggested an increase in mixing between the individual layers.

Originally, this was believed to have been an isolated incident; however, through the expansion of the original line-of-sight extinction dataset to include more than a full Martian year, *Moore et al.* (2016) revealed an apparent seasonality in the phenomenon as a subsequent dust event was witnessed approximately one Martian year later (following sol 650). In addition to the observed out-of-crater dust events, it is worth noting that another phenomenon was observed and briefly discussed in *Moore et al.* (2016) in which there exists a well-defined minimum in the Mastcam column extinction values to the extent that they overlap with the derived line-of-sight extinction values. This event was observed to

35

occur between sol 600 and sol 650; however, due to the limitation of the data utilized in *Moore et al.* (2016) only extending to sol 900, they were incapable of identifying a repetition of the event.

In order to assess the validity of the simplified methods of radiative transfer presented in *Moores et al.* (2015) and *Moore et al.* (2016) as well as whether the observed seasonal fluctuations of line-of-sight extinction described in *Moore et al.* (2016) are an artifact produced from the use of their simplified methods of radiative transfer, the three-dimensional radiative transfer model developed in this work was run over a variety of relevant scenarios. These scenarios were designed to not only provide an analysis of the publication methods and seasonal variations, but also to test the observation of the intra-crater depletion of dust loading as well as the existence of in-crater and out-of-crater atmospheric interactions.

Initially, the three-dimensional radiative transfer model was run using 1340 sols (just over two Martian years) of actual or interpolated Mastcam optical depth measurements. As discussed in the previous chapter, within the three-dimensional model, the Martian atmosphere was assumed to be well-mixed. Furthermore, the observation azimuth for this run of the three-dimensional model was held constant at $0°$, representing observations that are directed due north in order to mimic the Navcam observations demonstrated in *Moores et al.* (2015) and *Moore et al.* (2016). Following the specified run of the three-dimensional radiative transfer model, simulated values of line-of-sight extinction measurements were output for each individual sol. Figure 4.1 displays the resulting line-of-sight extinction measurements that were derived alongside the Mastcam column extinction observations as well as the ratio of the two individual datasets.

In regards to the line-of-sight extinction derived through the three-dimensional model, the calculated values displayed in Figure 4.1.a are seen to gradually follow the observed Mastcam column extinction trend similar to the observations in *Moores et al.* (2015) and *Moore et al.* (2016). However, the line-of-sight extinction values calculated for the case
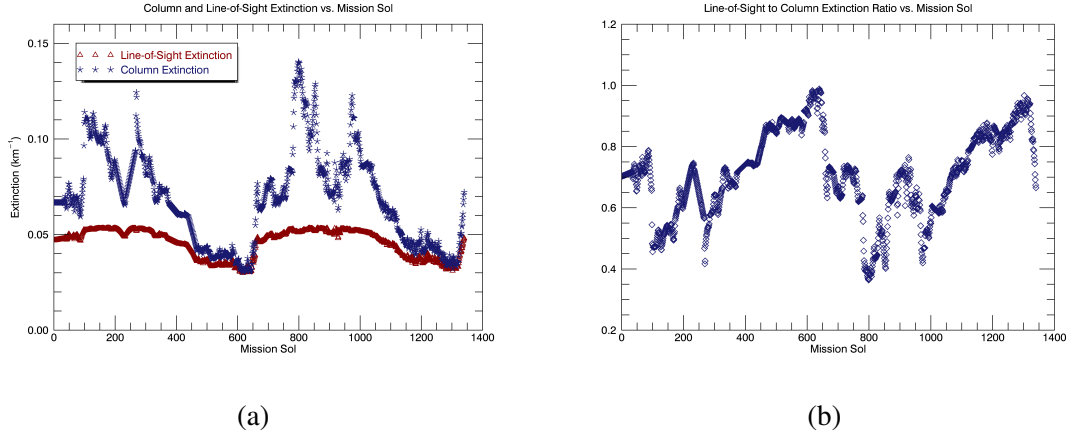
36

Figure 4.1: (a) Total column extinction (opacity per km) compared to model-derived line-of-sight extinction within the Gale Crater environment as a function of mission sol. The values displayed are the product of the average, interpolated Mastcam optical depth dataset that spans 1340 sols (just over 2 Martian years). (b) Ratio of the line-of-sight extinction to the column extinction displayed in (a) as a function of mission sol.

of a well-mixed atmosphere evidently fail to reasonably capture the substantial increases that coincide with the influence from the out-of-crater dust events, as they remain relatively flat throughout the duration of these observation periods. Furthermore, the model produced values of line-of-sight extinction also vary significantly in comparison to those observed in the publications. For instance, under the influence of a dust event, the three-dimensional model derived line-of-sight extinction values are approximately 66% of those observed while throughout the periods of substantially reduced extinctions, derived values can be near 50% greater than those observed. Corresponding with the variance in produced values, the ratio of the line-of-sight extinction to the column extinction also differs from that observed in the publications. As opposed to possessing values that are consistently lower than the observed column extinction by roughly 33% as addressed in *Moores et al.* (2015), the derived line-of-sight extinction to column extinction ratio deviates throughout the course of the Martian year as seen in Figure 4.1.b.
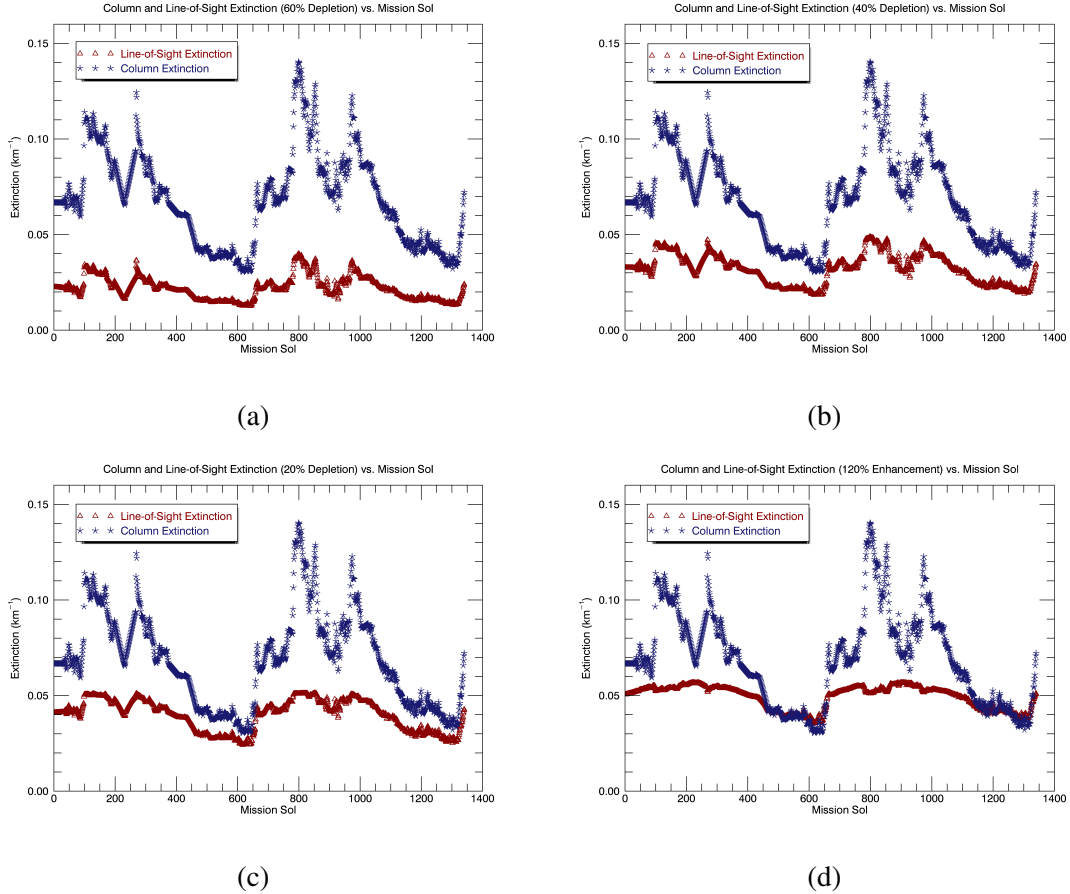
Figure 4.2: Individual plots of total column extinction (opacity per km) compared to model-derived line-of-sight extinction within Gale Crater for specified cases of in-crater opacity depletion and enhancement as a function of mission sol: (a) 60% depletion, (b) 40% depletion, (c) 20% depletion, (d) 120% enhancement. Each subplot displayed is a product of the average, interpolated Mastcam optical depth dataset.

To further investigate the collection of observed model-to-model anomalies for spurious seasonal variations, a divergence from the well-mixed assumption was taken in order to perform three-dimensional model runs that possessed cases of in-crater extinction depletion and enhancement. To conduct these model runs, it is assumed that the opacity within the boundary layer on each sol of the dataset is depleted or enhanced such that a specified percentile of the in-crater opacity is displaced into the atmosphere above the

crater or vice verse for the respective cases. In this work, four specific cases were selected for analysis (three cases of depletion (60%, 40%, 20%) and one of enhancement (120%)) and were similarly run over 1340 sols of actual or interpolated Mastcam optical depth measurements. Figure 4.2 conveys the model output line-of-sight extinction measurements for each individual case under consideration alongside the Mastcam total column extinction.

As expected, performing the runs of the cases of in-crater extinction depletion and enhancement altered the output line-of-sight extinction values such that they decreased and increased, respectively. Furthermore, perturbations of the original line-of-sight extinction plot shape can be seen in each of the four plots in Figure 4.2. Looking more closely at the plots of depletion, it is evident that as the larger steps of depletion are taken, the line-of-sight extinction continues to capture each individual variation exhibited in the Mastcam column extinction; thus, indicating that as the in-crater extinction is depleted, the line-of-sight extinction values come closer to directly matching it. On the contrary, the lone case of in-crater extinction enhancement produces a more flat plot, even appearing to oppose the increase in value when under the influence of observed dust activity.

The variations observed in the overall plot shape between the original line-of-sight extinction derived using the three-dimensional radiative transfer model (Figure 4.1.a) and those observed for the individual cases of depletion (Figure 4.2.a-c) can be explained by the fact that as the in-crater optical depth becomes small enough, the three-dimensional radiative transfer model begins to act similar to the methods in *Moores et al.* (2015) and *Moore et al.* (2016). This occurs due to the in-crater optical depth being so low that the source function term in the RTE is incredibly close to being a constant which matches the principal assumption originally established in *Moores et al.* (2015). Conversely, when the optical depth within Gale Crater is enhanced, the methods utilized in *Moores et al.* (2015) and *Moore et al.* (2016) are not compatible. Nevertheless, the individual methods of radiative transfer possess a commonality leading to believe that what is observed in the
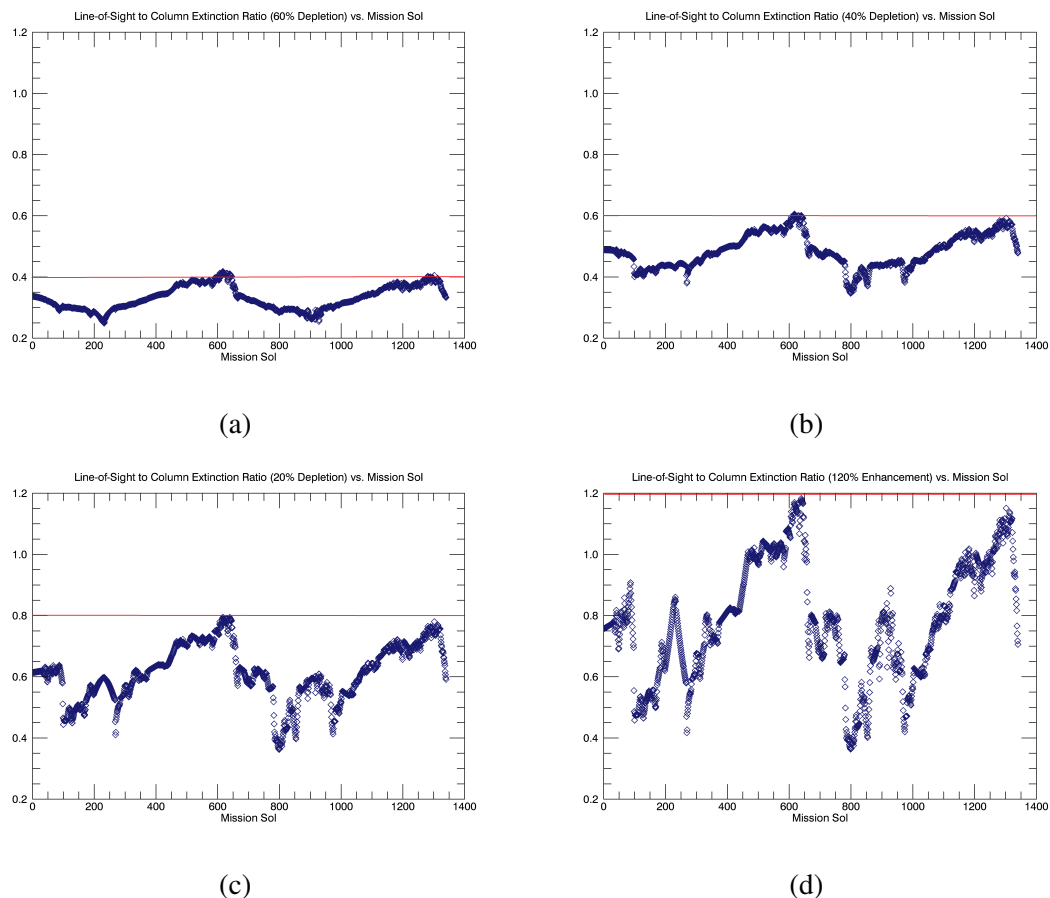
Figure 4.3: Individual plots of the ratio of the three-dimensional model derived line-of-sight extinction to total column extinction (opacity per km) within Gale Crater for specified cases of in-crater opacity depletion and enhancement as a function of mission sol where the horizontal red line indicates the anticipated ratio values for the respective depletion or enhancement case: (a) 60% depletion, (b) 40% depletion, (c) 20% depletion, (d) 120% enhancement. Each subplot displayed is a product of the average, interpolated Mastcam optical depth dataset.

publications is most likely a real seasonal effect through Martian atmospheric mixing interactions and not an artifact produced from the use of their simplified methods of radiative transfer.

Due to the deviation from *Moores et al.* (2015) observed in the line-of-sight to column extinction ratio in the initial model run, the ratio was consequently applied to the individual

cases of depletion and enhancement. Results of the line-of-sight to column extinction ratio for each specialized cases are displayed in Figure 4.3. As previously mentioned, *Moores et al.* (2015) observed a relatively constant ratio between the two measurements of extinction; therefore, the line-of-sight to column extinction ratio for the depletion and enhancement cases were also expected to be held constant with respect to the percentage deviation of the intra-crater opacity. However, as opposed to producing the anticipated ratio values (represented by the red horizontal line within each of the respective plots in Figure 4.3), the results of the ratios from the three-dimensional radiative transfer model once again displayed significant deviations; thus, exposing clear evidence that a limitation exists within the simplified methods of radiative transfer used in *Moores et al.* (2015) and *Moore et al.* (2016).

Through the use of various applicable scenarios, the analyses of the simplified radiative transfer model utilized in *Moores et al.* (2015) and *Moore et al.* (2016) demonstrate that the observation of the intra-crater depletion of near-surface dust loading as well as the seasonal variations of line-of-sight extinction due to Martian atmospheric interactions are likely real. However, the assortment of tests performed also reveal certain methodological weaknesses exposed through the ratio of the three-dimensional radiative transfer model derived line-of-sight extinction to the Mastcam observed total column extinction.

4.2 Geographic Inhomogeneity of Line-of-Sight Extinction

As previously mentioned in section 3.3, *Moore et al.* (2016) performed an analysis of line-of-sight extinction variability across the 45-degree Navcam frame in order to identify the existence of a geographic inhomogeneity. Their methods incorporated five regions along the crater rim that varied by increments of $9.6°$ to the east and west of the due north observation angle of $0°$. Through the analysis, it was determined that a spread of line-of-sight extinction was witnessed across the five regions varying by roughly $0.02\ km^{-1}$ on a

particular sol; thus, exceeding the calculated error estimates by an order of magnitude and further suggesting that the values obtained across the different regions are true variations of dust within the crater.

In order to evaluate if the geographic inhomogeneity in dust loading variability observed in *Moore et al.* (2016) was an artifact produced from the use of their simplified methods of radiative transfer, the three-dimensional radiative transfer model developed in this work was run using the average, interpolated Mastcam optical depth measurement dataset for two individual cases over a variety of relevant observation azimuths. This specific analysis made use of six observation azimuth angles ranging from $0°$ to $48°$, keeping the spacing between observation angles at $9.6°$ to remain consistent with the original study in the publication. Furthermore, within the three-dimensional radiative transfer model, the Martian atmosphere was held under the well-mixed assumption. Following the run of the three-dimensional radiative transfer model for the specified observation azimuths, Navcam simulated values of line-of-sight extinction measurements were output for each individual sol. The values of line-of-sight extinction that were output from the numerous model runs were observed to possess substantially small variance between the angular observations (on the order of 10^{-3}); thus, in order to understand the geographic differences across the defined observation frame, the model output was modified to illustrate the variations in percentile from the original observation angle of $0°$. The results for the initial three-dimensional model run encompassing the average, interpolated Mastcam optical depth dataset for the individual observation azimuths can be seen in Figure 4.4.

The main conclusion is that although lateral variations exist, they are small in comparison to the observed differences in *Moore et al.* (2016). It is also evident that the more significant the deviation from the due north observation angle, the more significant the variations become. Furthermore, the variations observed seem to alternate to negative values when the solar azimuth aim shifts from a northward position to southward ($0°$ to
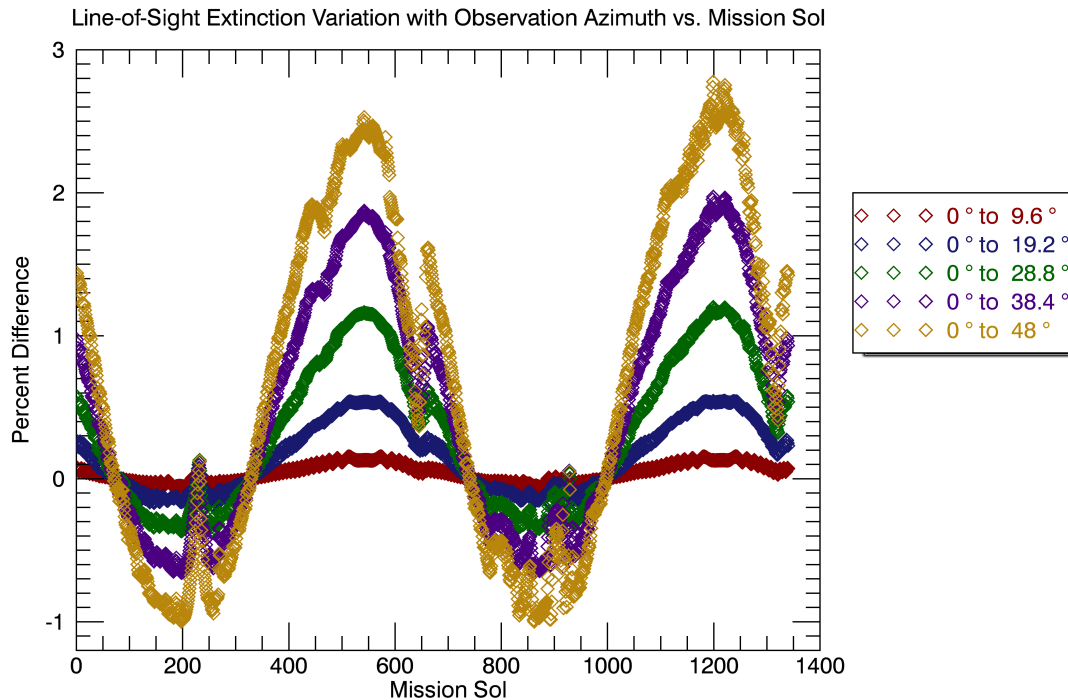
Figure 4.4: Line-of-sight extinction percentage variation with observation azimuth taken from the original observation angle of $0°$ as a function of mission sol. The data displayed are the product of the average, interpolated Mastcam optical depth dataset.

$180°$); thus, illustrating that their also exists a dependence on the solar geometry within the azimuthally-varied observations. In order to further investigate the solar geometric dependence in search of possible artifacts, a special case for observations that would occur in the early morning or evening hours was performed, deviating from the solely near-noon cases utilized in *Moore et al.* (2016).

In the AM/PM case, the solar geometry was set at $90°$ for the azimuth angle and $30°$ for the elevation angle; thus, eliminating the variance that was observed through the near-noon solar azimuth shifts. However, as can be seen in Figure 4.5, it is clear that there exists a seasonal variation similar to what was observed in the previous section coinciding with the presence of dust event activity or lack there of. The percent differences produced in
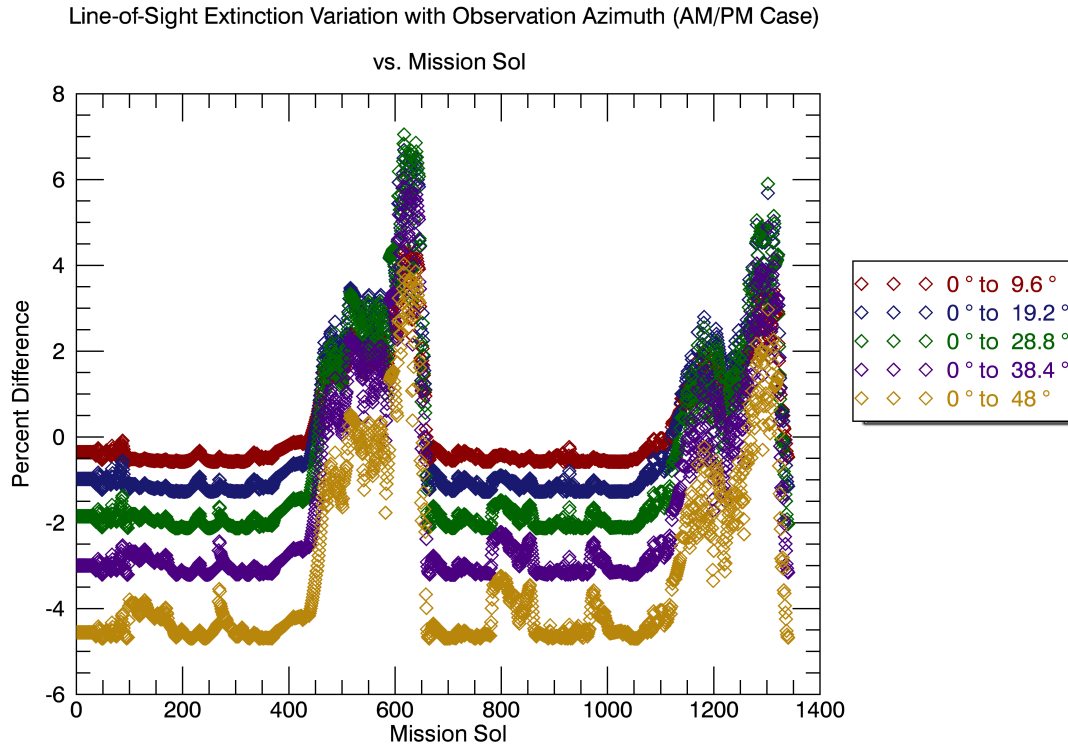
Figure 4.5: Line-of-sight extinction percentage variation with observation azimuth taken from the original observation angle of $0°$ as a function of mission sol. The data displayed are the product of the average, interpolated Mastcam optical depth dataset with solar geometry specified for the AM/PM case.

this case also, albeit still small in comparison to the observations from *Moore et al.* (2016), far exceed those observed in Figure 4.4. However, there exists an interesting observation such that the furthest deviation from the true north observation azimuth does not dominate the visible differences as illustrated in Figure 4.4.

Although the observations established using the three-dimensional radiative transfer model were relatively small in comparison to those in *Moore et al.* (2016), they were still capable of providing insight on the published observations. For instance, the errors from the lack of a three-dimensional radiative transfer model were small enough that the conclusions about the near-surface atmospheric dust loading from the original study remain

valid; therefore, the observed variations from the publication are not an artifact produced from the use of their simplified methods of radiative transfer. However, season-dependent biases exist and the geometry should be included more explicitly.

4.3 Limitations due to Wavelength Dependence

In *Moores et al.* (2015) and *Moore et al.* (2016), measurements of line-of-sight extinction were observed through the use of the MSL's Navcam. However, imagers aboard current missions possess (e.g. the MSL Mastcam), and future missions will possess (e.g. the InSight IDC and the Mars 2020 Mastcam-Z and EECams), the ability to capture images at various wavelengths. Furthermore, specific radiative property values including single-scattering albedo as well as the phase function of the atmospheric particles are relatively wavelength-dependent. Therefore, this work investigates the influence of varying observational wavelengths in the retrieval of line-of-sight extinction measurements in order to assess if the simplified methods of radiative transfer presented in *Moores et al.* (2015) and *Moore et al.* (2016) show wavelength-dependent variations.

In this analysis, the three-dimensional radiative transfer model developed in this work was run using the SSA and phase functions for the red (640 $\pm$ 44 nm), green (544 $\pm$ 38 nm), and blue (495 $\pm$ 37 nm) L0 color filters of the 34 mm left-mounted Mastcam. The filter-specific values replaced those defined for the Navcam that were utilized for the experiments detailed in the two previous sections. Through alterations of the SSA and phase function, it is possible to observe and directly identify the existence of possible limitations of the *Moores et al.* (2015) model equations at the camera relevant wavelengths. In order to observe the possible wavelength-dependent effects, the three-dimensional radiative transfer model was initially run using the average, interpolated Mastcam optical depth dataset for the three individual provided SSAs and phase functions. In these model runs, the observation azimuth was facing toward the north to allow for a direct comparison of the

45

(a)   (b)

(c)
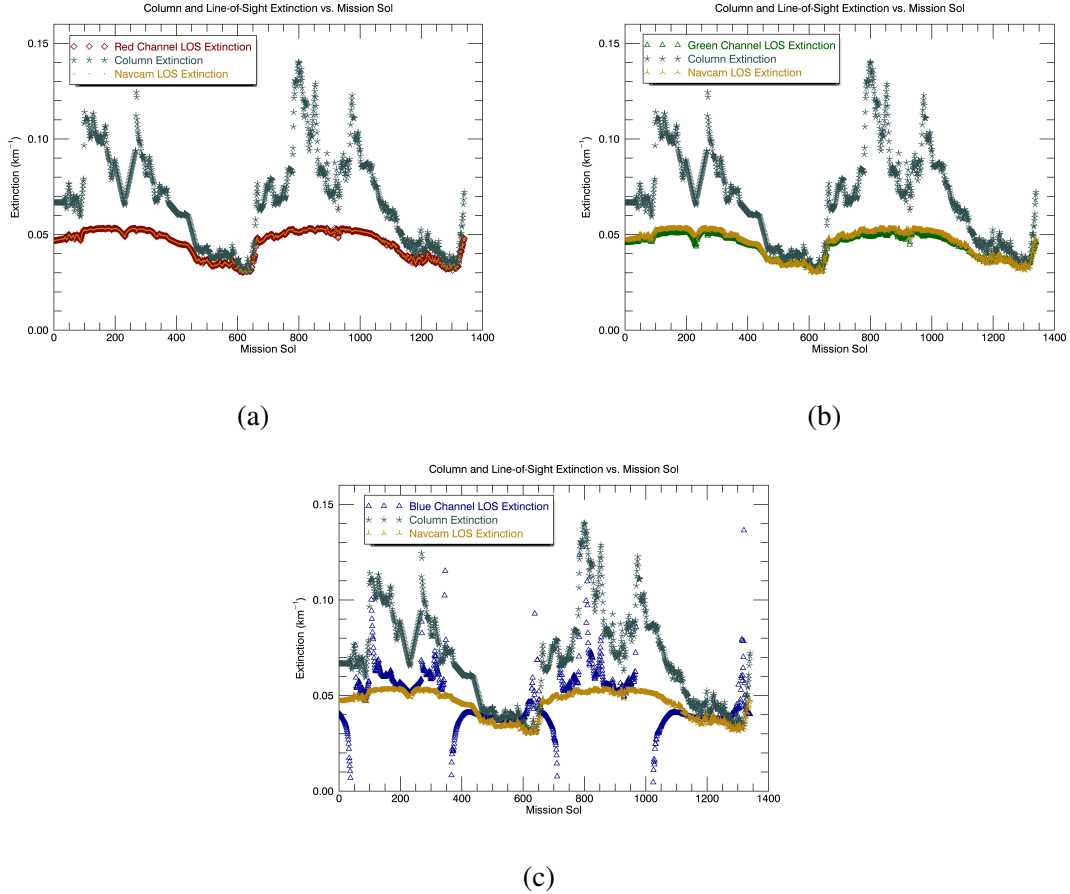
Figure 4.6: Total column extinction (opacity per km) compared to the model-derived red (a), green (b), and blue (c) channel filter line-of-sight extinction within Gale Crater as a function of mission sol. The original line-of-sight extinction from Figure 4.1.a for the Navcam filter is also included for reference. The data displayed are the product of the average, interpolated Mastcam optical depth dataset coinciding with the color respective SSA and phase functions.

various wavelength produced line-of-sight extinction measurements to what is originally observed for the Navcam relative inputs.

The results produced from the three individual runs can be seen in Figure 4.6.a-c, where each of the color-relative line-of-sight extinctions are plotted alongside the Mastcam column extinction as well as the Navcam derived line-of-sight extinctions. In Figure

4.6.a, the red channel line-of-sight derived observations in comparison to the Navcam observations possess very little deviation. This can be attributed to the fact that the red filter wavelength is comparable to the Navcam spectral range that spans 600 to 850 nm compared to 640 ± 44 nm for the red filter. Furthermore, similar to what was exhibited in the seasonality analysis, the red channel filter line-of-sight extinction fails at reasonably capturing the significant peaks in extinction associated with the increase of dust event activity that are observed within the column extinction. However, when column extinction measurement's attain their annual minimum, both the red filter and Navcam line-of-sight extinction correspond the the Mastcam observations; thus indicating a reasonable approach by *Moores et al.* (2015) and *Moore et al.* (2016) when the in-crater extinction values are relatively small.

The green channel filter line-of-sight extinction displayed in Figure 4.6.b possesses similar characteristics to those observed utilizing the red filter, such that the derived values of line-of-sight extinction do not follow the column extinction trend well when the seasonal peaks of dust events occur. Looking at Figure 4.6.b, it is clear that the green filter extinction values do not completely correspond to those observed for the Navcam. More specifically, the green filter extinctions are less than the Navcam relative values during the periods of higher column extinction. This can be attributed to the fact that the green filter wavelength range deviates out of the Navcam span of 650 to 800 nm to 544 ± 38 nm. Conversely, when the column extinction is seen to approach its annual minimum, the green filter extinction begins to coincide with the Navcam observed values. Therefore, coinciding with the red filter observations, this further indicates a reasonable approach by *Moores et al.* (2015) and *Moore et al.* (2016) when the in-crater extinction values are relatively small; however, it is evident that there exists some systematic caveats.

The line-of-sight extinction for the blue channel filter is illustrated in Figure 4.6.c. Looking at the plot, it is obvious that the blue channel line-of-sight extinction produced

47

through the three-dimensional radiative transfer model fails to resemble the Navcam line-of-sight extinction measurements as they possesses significant scattering and minimal characteristics in common. These artifacts highlight the limitations of the *Moores et al.* (2015) and *Moore et al.* (2016) model in regards the its wavelength dependence; more specifically, focusing on the four instances around the time in which the solar azimuth aim switches from a northward to southward position ($0°$ to $180°$), the plot of line-of-sight extinction resembles that of a limit of a function that becomes infinite. Furthermore, the *Moores et al.* (2015) and *Moore et al.* (2016) model also fails to convey extinction in the blue channel through the fact that the entirety of the input dataset could not be evaluated by the principal equation from the publications. This occurs because the measurement of intensity of the crater rim under the blue wavelength regime did not range between the observed radiance of the local ground and the Martian sky due to the tilted surface and solar geometry.

In order to further explore the limitations regarding the wavelength dependence of the three color channels, the surrogate dataset for *Moores et al.* (2015) and *Moore et al.* (2016) was used to observe a specified case with an arbitrary fixed depletion of 40%. The dataset was selected for this analysis as it possessed the solar azimuth and elevation angles for the Mastcam measurements that represent the Navcam retrievals in the published work in which the geometry seems to be a significant factor. The results from the radiative transfer model run for this specified case are displayed in Figure 4.7. The plot shows that the red channel extinction follows the trend of the Navcam extinction relatively uniformly. Furthermore, coinciding with the original case observations, the green channel filter extinction is observed to possess lower values of extinction in comparison to the Navcam measurements during periods of increased dust activity while agreeing with them during the lull in column extinction values.

The blue channel filter also possessed similar results to the case prior such that the
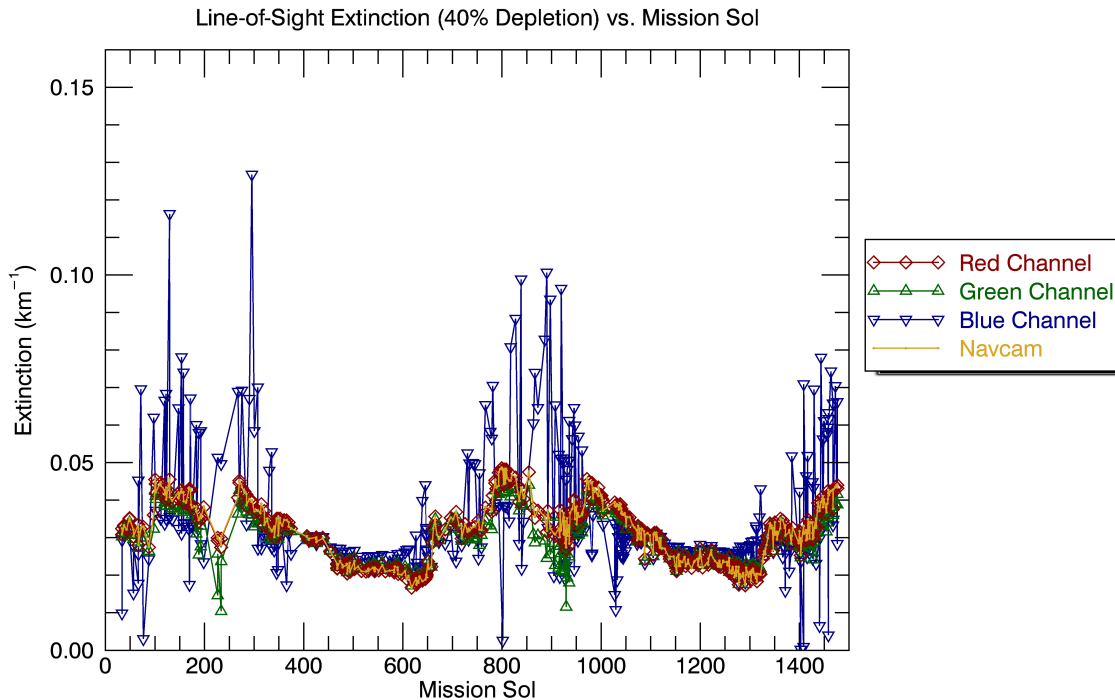
Figure 4.7: Line-of-sight extinction for the RGB channel filters with the Navcam line-of-sight extinction for reference as a function of mission sol. The data displayed were observed for a specified case with an arbitrarily fixed in-crater opacity depletion of 40%, utilizing the Mastcam optical depth dataset that serves as a surrogate to the published work.

extinction measurements possessed significant scattering, showing no signs of similarity to the Navcam extinction values. The blue channel line-of-sight extinction also differs from the previous observations as there are not any areas that tail off due to the 180° shifts in solar azimuth. Furthermore, following the model run, the complete dataset was not accounted for as 10% of the output produced was either a negative extinction or NaN value once again being attributed to the illumination of the tilted crater rim; thus, further highlighting the wavelength-dependent artifacts produced through the simplified radiative transfer method.

In order to investigate if there were any diurnal variations of wavelength dependence
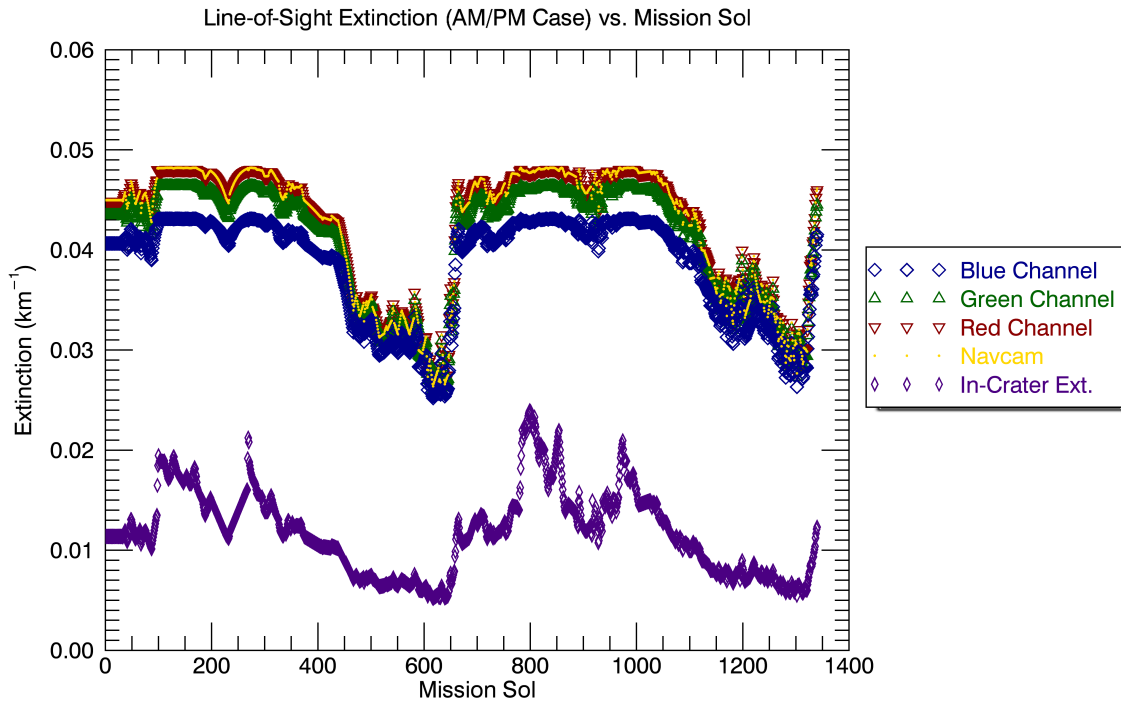
Figure 4.8: Line-of-sight extinction for the RGB channel filters with the Navcam line-of-sight extinction for reference as a function of mission sol. The data displayed are the product of the average, interpolated Mastcam optical depth dataset with solar geometry specified for the AM/PM case. The addition of the model input in-crater values of extinction are used to accentuate where the line-of-sight calculations do not reflect those observed by the Mastcam.

in the extinction measurements, the solar geometry was simulated for the early morning or late evening in the three-dimensional radiative transfer model. For the specified case, the input of the solar geometry was set at $90°$ for the azimuth angle and $30°$ for the elevation angle. The results from this run are displayed in Figure 4.8. The plot shows that red channel extinction once again follows the trend of the Navcam extinction. The green channel filter extinction, similar to the previous model runs, follows the Navcam trend but possesses lower values of extinction in comparison to the Navcam measurements during periods of increased dust activity while coinciding with the Navcam observations during

the annual minimum of column extinction values. The blue channel filter in this case captures the Navcam trend relatively well; however, the produced values of extinction deviate significantly from the Navcam values which can be attributed to the blue channel wavelength deviation from the Navcam spectral range. Furthermore, in regards to the blue channel filter, the provided dataset was captured in full as opposed to the prior model runs. Therefore, it can be inferred that the significant scattering artifact from the illumination of the tilted crater surface in the blue channel possesses diurnal variations.

Following the performance of numerous runs of the three-dimensional radiative transfer model to identify wavelength-dependent variations in the methods presented in *Moores et al.* (2015) and *Moore et al.* (2016), the results demonstrated a reasonable performance within the Navcam wavelength range. However, for shorter (more absorbing) wavelengths, significant scattering artifacts were observed that highlighted the limitations of the simplified methods of radiative transfer. The results demonstrate that the illumination and the reflection function of the crater rim become important sources of error that are highly correlated with geometry, which possess the capability to drive erroneous conclusions about the lateral, diurnal, or seasonal variations.

5. CONCLUSIONS

In order to assure that landed spacecraft for both present and future operations on Mars possess the robust capability of determining line-of-sight atmospheric optical depth, a three-dimensional radiative transfer model was developed to produce simulated atmospheric data that enabled the key conclusions from the simplified methodology for measuring dust content presented in *Moores et al.* (2015) and *Moore et al.* (2016) to be evaluated and validated while limiting the number of required free parameters. Through the conduction of numerous model runs and various analyses, the observations of the depletion of atmospheric dust loading near the surface within Gale Crater were determined to be accurate. In regards to the seasonal variations of line-of-sight extinction, the decrease in depletion during dust events is real, but there are systematic errors by inferring depletion is of comparable magnitude to other variations. Similarly, through the three-dimensional model runs analyzing the geographic inhomogeneity observed within *Moore et al.* (2016), the results indicated that the local-scale horizontal variability in line-of-sight extinction can most likely be attributed to Martian atmospheric interactions; however, the error bars presented in the publication are relatively optimistic.

Variations in the wavelength of the line-of-sight extinction derivations through the use of the red, green, and blue channel L0 color filters of the 34 mm left-mounted Mastcam in place of those defined for the Navcam proved that there exists limitations within the simplified methods of radiative transfer that are wavelength-dependent. More specifically, through model observations using the blue channel, it was evident that the limitations provided by the necessity to correct for the illumination of the tilted surface of the crater rim mountains possessed both diurnal and seasonal variations that were directly related to the solar geometry. Through these findings, future missions that plan on utilizing various

cameras to capture images and obtain line-of-sight opacity measurements can be aware of the limitations that the simplified methods of radiative transfer established in *Moores et al.* (2015) and *Moore et al.* (2016) possess. However, it is advisable to use more sophisticated radiative transfer methods.

REFERENCES

Allen, C. C., J. L. Gooding, M. Jercinovic, and K. Keil (1981), Altered basaltic glass: A terrestrial analog to the soil of Mars, *Icarus*, *45*(2), 347–369.

Baird, A., P. Toulmin, B. C. Clark, H. J. Rose, K. Keil, R. P. Christian, and J. L. Gooding (1976), Mineralogic and petrologic implications of Viking geochemical results from Mars: Interim report, *Science*, *194*(4271), 1288–1293.

Bell, J. (2008), *The Martian Surface: Composition, Mineralogy and Physical Properties*, Cambridge University Press, New York City.

Bell, J., H. McSween, J. Crisp, R. Morris, S. Murchie, N. Bridges, J. Johnson, D. Britt, M. Golombek, H. Moore, et al. (2000), Mineralogic and compositional properties of Martian soil and dust: Results from Mars Pathfinder, *Journal of Geophysical Research: Planets*, *105*(E1), 1721–1755.

Bell, J., J. Maki, G. Mehall, M. Ravine, and M. Caplinger (2014), Mastcam-Z: A geologic, stereoscopic, and multispectral investigation on the NASA Mars-2020 rover, in *International Workshop on Instrumentation for Planetary Missions, Greenbelt, Maryland*.

Cantor, B. A. (2007), MOC observations of the 2001 Mars planet-encircling dust storm, *Icarus*, *186*(1), 60–96, doi:10.1016/j.icarus.2006.08.019.

Cantor, B. A., P. B. James, M. Caplinger, and M. J. Wolff (2001), Martian dust storms: 1999 Mars Orbiter Camera observations, *Journal of Geophysical Research: Planets*, *106*(E10), 23,653–23,687.

Cantor, B. A., K. M. Kanak, and K. S. Edgett (2006), Mars Orbiter Camera observations of Martian dust devils and their tracks (September 1997 to January 2006) and evaluation of theoretical vortex models, *Journal of Geophysical Research: Planets*, *111*(E12).

Colburn, D., J. Pollack, and R. Haberle (1989), Diurnal variations in optical depth at Mars,

Icarus, *79*(1), 159–189.

Dayou, J., J. H. W. Chang, and J. Sentian (2014), Ground-based aerosol optical depth measurements, in *Ground-Based Aerosol Optical Depth Measurement Using Sunphotometers*, pp. 9–30, Springer, Singapore.

Fenton, L., D. Reiss, M. Lemmon, B. Marticorena, S. Lewis, and B. Cantor (2016), Orbital observations of dust lofted by daytime convective turbulence, *Space Science Reviews*, pp. 1–54.

Ferguson, D. C., J. C. Kolecki, M. W. Siebert, D. M. Wilt, and J. R. Matijevic (1999), Evidence for Martian electrostatic charging and abrasive wheel wear from the Wheel Abrasion Experiment on the Pathfinder Sojourner rover, *Journal of geophysical research*, *104*(E4), 8747–8789.

Forget, F., F. Hourdin, C. Hourdin, and O. Talagrand (1999), Simulations of the Martian seasonal dust cycle with a general circulation model, in *4th International Conference on Mars, abstract 6206*.

Gierasch, P. J., and R. M. Goody (1972), The effect of dust on the temperature of the Martian atmosphere, *Journal of the Atmospheric Sciences*, *29*(2), 400–402.

Goetz, W., K. Leer, H. P. Gunnlaugsson, P. Bartlett, B. Basso, J. Bell, P. Bertelsen, C. S. Binau, P. C. Chu, S. Gorevan, M. F. Hansen, S. F. Hviid, K. M. Kinch, G. Klingelhöfer, A. Kusack, M. B. Madsen, D. W. Ming, R. V. Morris, E. Mumm, T. Myrick, M. Olsen, S. W. Squyres, J. Wilson, and A. Yen (2008), Search for magnetic minerals in Martian rocks: Overview of the Rock Abrasion Tool (RAT) magnet investigation on Spirit and Opportunity, *Journal of Geophysical Research*, *113*(E5), doi:10.1029/2006JE002819.

Greeley, R., P. L. Whelley, R. E. Arvidson, N. A. Cabrol, D. J. Foley, B. J. Franklin, P. G. Geissler, M. P. Golombek, R. O. Kuzmin, G. A. Landis, et al. (2006), Active dust devils in Gusev Crater, Mars: Observations from the Mars Exploration Rover Spirit, *Journal of Geophysical Research: Planets*, *111*(E12).

Gunn, M. D., and C. R. Cousins (2016), Mars surface context cameras past, present, and future, *Earth and Space Science*, *3*(4), doi:10.1002/2016EA000166.

Haberle, R. M., J. B. Pollack, J. R. Barnes, R. W. Zurek, C. B. Leovy, J. R. Murphy, H. Lee, and J. Schaeffer (1993), Mars atmospheric dynamics as simulated by the NASA Ames general circulation model: 1. the zonal-mean circulation, *Journal of Geophysical Research: Planets*, *98*(E2), 3093–3123.

Hanel, R., B. Conrath, W. Hovis, V. Kunde, P. Lowman, W. Maguire, J. Pearl, J. Pirraglia, C. Prabhakara, B. Schlachman, G. Levin, P. Straat, and T. Burke (1972), Investigation of the Martian environment by infrared spectroscopy on Mariner 9, *Icarus*, *17*(2), 423–442, doi:10.1016/0019-1035(72)90009-7.

Hansen, J. E., and L. D. Travis (1974), Light scattering in planetary atmospheres, *Space Science Reviews*, *16*(4), 527–610, doi:10.1007/bf00168069.

Heavens, N., M. Richardson, A. Kleinböhl, D. Kass, D. McCleese, W. Abdou, J. Benson, J. Schofield, J. Shirley, and P. Wolkenberg (2011), The vertical distribution of dust in the Martian atmosphere during northern spring and summer: Observations by the Mars Climate Sounder and analysis of zonal average vertical dust profiles, *Journal of Geophysical Research: Planets*, *116*(E4).

Hoekzema, N., M. Garcia-Comas, O. Stenzel, E. Petrova, N. Thomas, W. Markiewicz, K. Gwinner, H. Keller, and W. Delamere (2011), Retrieving optical depth from shadows in orbiter images of Mars, *Icarus*, *214*(2), 447–461.

Hviid, S. F., M. B. Madsen, H. P. Gunnlaugsson, W. Goetz, J. M. Knudsen, R. B. Hargraves, P. Smith, D. Britt, A. R. Dinesen, C. T. Mogensen, M. Olsen, C. T. Pedersen, and L. Vistisen (1997), Magnetic properties experiments on the Mars Pathfinder lander: Preliminary results, *Science*, *278*(5344), 1768–1770, doi:10.1126/science.278.5344.1768.

Johnson, J. R., W. M. Grundy, and M. T. Lemmon (2003), Dust deposition at the Mars Pathfinder landing site: Observations and modeling of visible/near-infrared spectra,

Icarus, *163*(2), 330–346.

Kahanpää, H., M. de la Torre Juarez, J. Moores, N. Rennó, S. Navarro, R. Haberle, M.-P. Zorzano, J. Martín Torres, J. Verdasca, A. Lepinette, J. A. Rodriguez-Manfredi, J. Gómez-Elvira, The REMS Team, and MSL Science Team (2013), Convective vortices in Gale Crater, in *EGU General Assembly*, vol. 15, pp. EGU2013–9455.

Kahanpää, H., C. Newman, J. Moores, M.-P. Zorzano, J. Martín-Torres, S. Navarro, A. Lepinette, B. Cantor, M. T. Lemmon, P. Valentín-Serrano, A. Ullán, and W. Schmidt (2016), Convective vortices and dust devils at the MSL landing site: Annual variability, *Journal of Geophysical Research: Planets*, *121*(8), doi:10.1002/2016JE005027.

Kahre, M. A., J. R. Murphy, and R. M. Haberle (2006), Modeling the Martian dust cycle and surface dust reservoirs with the NASA Ames general circulation model, *Journal of Geophysical Research: Planets*, *111*(E6).

Kuhn, W. R., and S. K. Atreya (1979), Solar radiation incident on the Martian surface, *Journal of Molecular Evolution*, *14*(1), 57–64, doi:10.1007/BF01732367.

Lemmon, M. (2010), Martian cirrus-like hazes at the Phoenix landing site, in *41st Lunar and Planetary Science Conference*.

Lemmon, M. (2014), The Mars Science Laboratory optical depth record, *LPI Contributions*, *1791*, 1338.

Lemmon, M., M. Wolff, M. Smith, R. Clancy, D. Banfield, G. Landis, A. Ghosh, P. Smith, N. Spanovich, B. Whitney, et al. (2004), Atmospheric imaging results from the Mars Exploration Rovers: Spirit and Opportunity, *Science*, *306*(5702), 1753–1756.

Lemmon, M. T., M. J. Wolff, J. F. Bell, M. D. Smith, B. A. Cantor, and P. H. Smith (2015), Dust aerosol, clouds, and the atmospheric optical depth record over 5 Mars years of the Mars Exploration Rover mission, *Icarus*, *251*, 96–111.

Mahaffy, P. R., C. R. Webster, S. K. Atreya, H. Franz, M. Wong, P. G. Conrad, D. Harpold, J. J. Jones, L. A. Leshin, H. Manning, et al. (2013), Abundance and isotopic composition

of gases in the Martian atmosphere from the Curiosity rover, *Science*, *341*(6143), 263–266.

Maki, J., D. Thiessen, A. Pourangi, P. Kobzeff, T. Litwin, L. Scherr, S. Elliott, A. Dingizian, and M. Maimone (2012), The Mars Science Laboratory Engineering Cameras, *Space Science Reviews*, *170*(1), 77–93, doi:10.1007/s11214-012-9882-4.

Maki, J. N., J. F. Bell, K. E. Herkenhoff, S. W. Squyres, A. Kiely, M. Klimesh, M. Schwochert, T. Litwin, R. Willson, A. Johnson, M. Maimone, E. Baumgartner, A. Collins, M. Wadsworth, S. T. Elliot, A. Dingizian, D. Brown, E. C. Hagerott, L. Scherr, R. Deen, D. Alexander, and J. Lorre (2003), Mars Exploration Rover Engineering Cameras, *Journal of Geophysical Research: Planets*, *108*(E12), 8071, doi: 10.1029/2003JE002077.

Maki, J. N., C. M. McKinney, R. G. Sellar, D. S. Copley-Woods, D. C. Gruel, D. L. Nuding, M. Valvo, T. Goodsall, J. McGuire, and T. E. Litwin (2016), Enhanced Engineering Cameras (EECAMs) for the Mars 2020 rover, *3rd International Workshop on Instrumentation for Planetary Missions*, p. 4132.

Malin, M., K. Edgett, E. Jensen, and L. Lipkaman (2013), Mast Camera (Mastcam), Mars Hand Lens Imager (MAHLI), and Mars Descent Imager (MARDI) Experiment Data Record (EDR) and Reduced Data Record (RDR) PDS data products, version 1.2, *Mars Science Laboratory Project Software Interface Specification (SIS)*.

Malin, M. C., J. F. Bell, III, J. Cameron, W. E. Dietrich, K. S. Edgett, B. Hallet, K. E. Herkenhoff, M. T. Lemmon, T. J. Parker, R. J. Sullivan, D. Y. Sumner, P. C. Thomas, E. E. Wohl, M. A. Ravine, M. A. Caplinger, and J. N. Maki (2005), The Mast Cameras and Mars Descent Imager (MARDI) for the 2009 Mars Science Laboratory, in *36th Annual Lunar and Planetary Science Conference*, *Lunar and Planetary Science Conferenc*, vol. 36.

Markiewicz, W., R. Sablotny, H. Keller, N. Thomas, D. Titov, and P. Smith (1999), Optical

properties of the Martian aerosols as derived from Imager for Mars Pathfinder midday sky brightness data, *Journal of Geophysical Research: Planets*, *104*(E4), 9009–9017.

Markiewicz, W., E. Petrova, N. Hoekzema, A. Inada, H. Keller, K. Gwinner, H. Hoffmann, and G. Neukum (2005), The retrieval of atmospheric optical depth and surface albedo of Mars from the brightness of surface shadows in the HRSC images, in *Geophysical Research Abstracts*, vol. 7, p. 05193.

Martin, L. J., and R. W. Zurek (1993), An analysis of the history of dust activity on Mars, *Journal of Geophysical Research: Planets*, *98*(E2), 3221–3246.

Melnik, O., and M. Parrot (1998), Electrostatic discharge in Martian dust storms, *Journal of Geophysical Research: Space Physics*, *103*(A12), 29,107–29,117.

Mendrok, J. (2006), The SARTre model for radiative transfer in spherical atmospheres and its application to the derivation of cirrus cloud properties, Ph.D. thesis, Freie Universitat Berlin.

Mishra, M. K., P. Chauhan, R. Singh, S. M. Moorthi, and S. S. Sarkar (2016), Estimation of dust variability and scale height of atmospheric optical depth (AOD) in the Valles Marineris on Mars by Indian Mars Orbiter Mission (MOM) data, *Icarus*, *265*, 84–94, doi:10.1016/j.icarus.2015.10.017.

Möller, D. (2014), *Chemistry of the Climate System*, De Gruyter, Berlin.

Montabone, L., F. Forget, E. Millour, R. Wilson, S. Lewis, B. Cantor, D. Kass, A. Kleinböhl, M. Lemmon, M. Smith, et al. (2015), Eight-year climatology of dust optical depth on Mars, *Icarus*, *251*, 65–95.

Moore, C. A., J. E. Moores, M. T. Lemmon, S. C. Rafkin, R. Francis, J. Pla-García, R. M. Haberle, M.-P. Zorzano, F. J. Martín-Torres, J. R. Burton, et al. (2016), A full Martian year of line-of-sight extinction within Gale Crater, Mars as acquired by the MSL Navcam through sol 900, *Icarus*, *264*, 102–108.

Moores, J. E., M. T. Lemmon, H. Kahanpää, S. C. Rafkin, R. Francis, J. Pla-Garcia,

K. Bean, R. Haberle, C. Newman, M. Mischna, et al. (2015), Observational evidence of a suppressed planetary boundary layer in northern Gale Crater, Mars as seen by the Navcam instrument onboard the Mars Science Laboratory rover, *Icarus*, *249*, 129–142.

Morris, R. V., D. Golden, J. F. Bell, H. V. Lauer, and J. B. Adams (1993), Pigmenting agents in Martian soils: Inferences from spectral, Mössbauer, and magnetic properties of nanophase and other iron oxides in Hawaiian palagonitic soil PN-9, *Geochimica et cosmochimica acta*, *57*(19), 4597–4609.

Mulholland, D. P., P. L. Read, and S. R. Lewis (2013), Simulating the interannual variability of major dust storms on Mars using variable lifting thresholds, *Icarus*, *223*(1), 344–358.

Pierrehumbert, R. T. (2010), *Principles of Planetary Climate*, Cambridge University Press, New York City.

Pollack, J. B., M. E. Ockert-Bell, and M. K. Shepard (1995), Viking lander image analysis of Martian atmospheric dust, *Journal of Geophysical Research: Planets*, *100*(E3), 5235–5250.

Putzig, N. E., and M. T. Mellon (2007), Apparent thermal inertia and the surface heterogeneity of Mars, *Icarus*, *191*(1), 68–94, doi:10.1016/j.icarus.2007.05.013.

Read, P., S. Lewis, and D. Mulholland (2015), The physics of Martian weather and climate: A review, *Reports on Progress in Physics*, *78*(12), 125,901.

Smith, M. D. (2004), Interannual variability in TES atmospheric observations of Mars during 1999–2003, *Icarus*, *167*(1), 148–165.

Smith, M. D. (2009), THEMIS observations of Mars aerosol optical depth from 2002–2008, *Icarus*, *202*(2), 444–452.

Smith, M. D., M.-P. Zorzano, M. Lemmon, J. Martín-Torres, and T. Mendaza de Cal (2016), Aerosol optical depth as observed by the Mars Science Laboratory REMS UV photodiodes, *Icarus*, *280*, 234–248, doi:10.1016/j.icarus.2016.07.012.

Spiga, A., and F. Forget (2009), A new model to simulate the Martian mesoscale and microscale atmospheric circulation: Validation and first results, *Journal of Geophysical Research: Planets*, *114*(E2).

Sportisse, B. (2010), Atmospheric radiative transfer, in *Fundamentals in Air Pollution*, pp. 45–92, Springer, Dordrecht.

Stamnes, K., S. C. Tsay, W. Wiscombe, and I. Laszlo (2000), *DISORT, a General-Purpose Fortran Program for Discrete-Ordinate-Method Radiative Transfer in Scattering and Emitting Layered Media: Documentation of Methodology*.

Tomasko, M. G., L. Doose, M. Lemmon, P. Smith, and E. Wegryn (1999), Properties of dust in the Martian atmosphere from the Imager on Mars Pathfinder, *Journal of Geophysical Research: Planets*, *104*(E4), 8987–9007.

Tyler, D., Jr., and J. R. Barnes (2013), Mesoscale modeling of the circulation in the Gale Crater region: An investigation into the complex forcing of convective boundary layer depths, *International Journal of Mars Science and Exploration*, *8*, 58–77, doi:10.1555/mars.2013.0003.

Vasavada, A. R., A. Chen, J. R. Barnes, P. D. Burkhart, B. A. Cantor, A. M. Dwyer-Cianciolo, R. L. Fergason, D. P. Hinson, H. L. Justh, D. M. Kass, S. R. Lewis, M. A. Mischna, J. R. Murphy, S. C. R. Rafkin, D. Tyler, and P. G. Withers (2012), Assessment of environments for Mars Science Laboratory entry, descent, and surface operations, *Space Science Reviews*, *170*(1), 793–835, doi:10.1007/s11214-012-9911-3.

Vincendon, M., Y. Langevin, F. Poulet, J.-P. Bibring, and B. Gondet (2007), Recovery of surface reflectance spectra and evaluation of the optical depth of aerosols in the near-IR using a Monte Carlo approach: Application to the OMEGA observations of high-latitude regions of Mars, *Journal of Geophysical Research*, *112*(E8), E08S13, doi: 10.1029/2006JE002845.

Wendisch, M., and P. Yang (2012), *Theory of Atmospheric Radiative Transfer*, Physics

textbook, Wiley, Weinheim.

Wiscombe, W. J. (1977), The delta-M method: Rapid yet accurate radiative flux calculations for strongly asymmetric phase functions, *Journal of the Atmospheric Sciences*, *34*(9), 1408–1422, doi:10.1175/1520-0469(1977)034<1408:TDMRYA>2.0.CO;2.

Wolff, M., M. Smith, R. Clancy, R. Arvidson, M. Kahre, F. Seelos, S. Murchie, and H. Savijärvi (2009), Wavelength dependence of dust aerosol single scattering albedo as observed by the Compact Reconnaissance Imaging Spectrometer, *Journal of Geophysical Research: Planets*, *114*(E2).

Zhai, Y., S. Cummer, and W. Farrell (2006), Quasi-electrostatic field analysis and simulation of Martian and terrestrial dust devils, *Journal of Geophysical Research: Planets*, *111*(E6).

Zurek, R. W., and L. J. Martin (1993), Interannual variability of planet-encircling dust storms on Mars, *Journal of Geophysical Research: Planets*, *98*(E2), 3247–3259.